Ocean Engineering 332 (2025) 121354

Contents lists available at ScienceDirect

Ocean Engineering

journal homepage: www.elsevier.com/locate/oceaneng

Research paper

Numerical analysis of multiple-chamber OWCs efficiency using a fast PTO modelling approach in OpenFOAM

J.F.M. Gadelho [a], G. Barajas [b], J.L. Lara [b], C. Guedes Soares [a,*]

[a] Centre for Marine Technology and Ocean Engineering (CENTEC), Instituto Superior Técnico, Universidade de Lisboa, Portugal
[b] IHCantabria - Instituto de Hidráulica Ambiental de La Universidad de Cantabria, Santander, Spain

ARTICLE INFO

Keywords:
Oscillating water column
NWT
OpenFOAM
PTO modelling
Triple-chamber OWC

ABSTRACT

A Numerical Wave Tank is developed within the OpenFOAM® environment to study a Triple-Chamber Oscillating Water Column using a fast PTO modelling technique. Three PTO modelling approaches are studied: the first physically represents the damping holes in the experiments, and two others use damping numerical regions; the second models the PTO as a porous media inducing momentum loss, and in the third, the PTO is modelled by a sink of momentum induced by a linear velocity damping term. The calibration and validation of the Numerical Wave Tank are done for a Dual-Chamber Oscillating Water Column using the three approaches. Approaches 2 and 3, which model the PTO as numerical regions, were faster, up to 40 %, compared to the real holes approach. Results show that including a third chamber in the Triple-Chamber has neglectable efficiency advantages for the lower damping PTO conditions. For the higher PTO damping conditions, the Triple-Chamber performs worse, having a primary efficiency of around 45 % compared to the 60 % from the Dual-Chamber. In this case, Approaches 2 and 3 were faster, up to 60 %, compared to the real holes approach in the Triple-Chamber case.

1. Introduction

Fossil fuels have an increasing negative impact on the environment and raise global concerns about their sustainability. Renewable energies, and ocean energy, in particular, are the sustainable alternative. Due to its wide availability and energy prediction over the years, ocean energy extraction has been extensively studied, and several devices have been installed (Falcão et al., 2019; Guedes Soares et al., 2012; Magagna et al., 2019). Compared to other Wave Energy Converters (WECs), Oscillating Water Column (OWC) has become a leading technology in this field. Unfortunately, to become economically viable, OWCs still face several challenges. Their global efficiency must be improved for a wider variety of wave conditions.

To overcome these challenges, it was discovered that by adding a step in front of a classic OWC, its efficiency significantly increased (Ning et al., 2019a; Rezanejad et al., 2019a, 2019b; Rezanejad and Guedes Soares, 2014, 2018). The authors explain that the stepped bottom OWC device can be compared to a dual-mass oscillatory system, where hydrodynamic resonance effects amplify the captured energy. Unfortunately, this resonance effect only works for a narrow wave frequency. To widen the sea states where an OWC is highly efficient, several authors used a multi-chamber system. (Rezanejad et al., 2015; Ning et al., 2017, 2019b). They proved that the different resonance frequencies of the chambers lead to a global improvement of the efficiency for wider sea states compared to a classic single-chamber OWC.

The natural evolution of the design of fixed OWCs is the combination of stepped OWCs with multi-chambers, which permits the extraction of more energy for a broader range of wave periods (Gadelho et al., 2024a). In this matter, Rezanejad et al. (2020), performed simulations with a low-fidelity numerical code of a stepped dual-chamber onshore OWC. They concluded that its efficiency is near 75 % for almost all of the tested wave periods. In the follow-up of this study, experimental (Gadelho et al., 2024b) and high-fidelity numerical (Gadelho and Guedes Soares, 2022) studies were developed interactively. This means that the first experimental results were used to calibrate and validate the Computational Fluid Dynamics (CFD) numerical model. Then, simulations with the CFD model showed that increasing the PTO damping led to a rise of the efficiency by up to 60 %, which permitted a new experimental campaign. The later experimental results confirmed that the efficiency curve is identical to the CFD model, but the maximum efficiency recorded was about 40 %.

By adding a multi-chamber configuration to the OWC device, several

* Corresponding author.
E-mail address: c.guedes.soares@centec.tecnico.ulisboa.pt (C. Guedes Soares).

https://doi.org/10.1016/j.oceaneng.2025.121354
Received 20 January 2025; Received in revised form 13 April 2025; Accepted 22 April 2025
Available online 9 May 2025
0029-8018/© 2025 The Authors. Published by Elsevier Ltd. This is an open access article under the CC BY-NC-ND license (http://creativecommons.org/licenses/by-nc-nd/4.0/).

authors reported an improvement of the global efficiency compared to classic single-chamber OWCs. Zhao et al. (2021) conducted experiments with several configurations of a combined multi-chamber OWC breakwater. They observed that the multi-chamber cases are more efficient in extracting wave power. Mia et al. (2022) made CFD simulations with multi-chamber OWCs. They conclude that a triple-chamber-triple-turbine configuration is more efficient than a dual-chamber-dual-turbine configuration. Kim and Nam (2022) studied numerically multi-chamber OWCs. They also found out that the case with multi-chambers conducts an increase in efficiency as well as less wave energy conversion variability.

Another challenge in the design of multi-chamber OWCs is to develop tools and methodologies that can both be fast and accurate. They must also give a certain degree of confidence in decision-making when going for a full-scale prototype. Major deviations from the expectation compared to reality can lead to huge economic losses. To assess the key physical processes behind OWCs, experimental wave tanks have been widely used. For example, Sarmento (1992) performed experiments on an OWC in an experimental tank to prove the oscillating surface pressure theory applied to an OWC. Rosa-Santos et al. (2019) performed experiments on a hybrid WEC integrated into a harbour breakwater. They concluded that integrating the hybrid WEC in a harbour breakwater is not harmful to its stability and reduces overtopping. Unfortunately, these kinds of tests require massive installations and availability and can be very costly.

With the increase in computational resources' availability, CFD numerical models have become very popular in industry and academia to simulate multiple extreme events accurately. CFD simulations have evident advantages compared to experimental tests. These do not need very big installations, the simulations can be automated to run for several days without the intervention of the user, several numerical sensors can be installed without affecting the flow, etc …. In this case, a reliable numerical study of an OWC model can be executed faster and cheaper compared to an experimental study. However, properly calibrating and validating these numerical models with experimental data is critical.

In this matter, numerous numerical studies of OWCs have been published over the last 10 years. López et al. (2014) used a two-dimensional numerical model that use the Reynolds-averaged Navier–Stokes (RANS) equations to optimise the PTO damping for an OWC. Iturrioz et al. (2014) used IH-2VOF, which is a two-dimensional RANS numerical model, to help with the design of OWC devices and study its economic feasibility. Later, Iturrioz et al. (2015) validated OpenFOAM to study 3D OWC devices. Deng et al. (2020) also used OpenFOAM to study an OWC combined with a breakwater. They conclude that the device's maximum efficiency is around 40 %. Batlle Martin et al. (2023) compared numerical and experimental results of wave-induced loads on a large-scale OWC. They conclude that, for some values of PTO damping, the numerical model needs to correctly simulate compressible effects inside the chamber to reproduce the extreme wave loads recorded in the experiments.

However, a common challenge that can be identified in these numerical studies is the difficulty of adequately modelling the action of the PTO. Usually, to reproduce the action of the PTO damping, in the experiments, a hole is applied on the top of the chamber. By changing its area, it is possible to model different PTO damping. The same method can be used in CFD simulations. However, generally, the orifice is so small compared to the rest of the domain that the mesh resolution in this area becomes quite challenging to define. This means that the cell size in this area must be excessively small compared to the rest of the domain and it becomes a "bottleneck" in terms of computational efforts. To maintain reasonable accuracy and stability, simulations will take excessive time.

Examples of alternative PTO definitions in CFD models have been reported by several authors. For example, Kamath et al. (2015) modelled the PTO damping of an OWC using porous layers in REEF3D. They observed that the PTO damping greatly influences the OWC's efficiency. Dimakopoulos et al. (2015) used OpenFOAM to characterise the flow exchange through the PTO of an OWC. They compared their numerical results with experiments and concluded that they agree very well when compressibility effects are neglected for low-damping PTO configurations. Xu and Huang (2019) modelled the nonlinearity of the PTO installed in a circular OWC using a CFD model. They conclude that the model can accurately describe the air and water flows inside OWC and the Free Surface Elevations (FSEs) in its vicinity.

However, none of the above-mentioned research studies make use of numerical regions to model the PTO in the OpenFOAM environment. In the present work, a novel methodology for designing multi-chamber OWCs using a fast CFD approach to model the PTO damping in the OpenFOAM environment is presented. Three numerical methods are described and characterised in terms of accuracy and computational costs to model the PTO damping: In the first approach, the PTO is modelled as an orifice identical to the experiments; in the second approach, the PTO is modelled as a porous media using Volume Averaged Reynolds-Averaged Navier-Stokes (VARANS) equations; while in the third approach, it is modelled directly by a loss of momentum due to an artificial drag force. A Numerical Wave Tank (NWT) for a Dual-Chamber OWC (DCOWC) is presented, calibrated, validated, and later applied to a Triple-Chamber OWC (TCOWC). The efficiency of the dual- and triple-chamber OWCs is quantified and analysed. The air pressures and FSEs inside the chambers are also presented.

The paper structure is as follows. In the second section, the methodology is presented, and the CFD numerical model is described in section 3. Section 4 presents a NWT that is calibrated and validated for a DCOWC. In the fifth section, the NWT is applied to analyse the efficiency of the triple-chamber OWC. In section six the concluding remarks and future work are presented. Finally, the appendix section presents snapshots of the CFD simulations for the dual- and triple-chamber OWCs.

2. Methodology

A wide variety of methodologies to design multi-chamber OWCs have been published over the years. Generally, these methodologies do not consider all the input parameters, such as installation characteristics (for example, long-term local sea state) or PTO characteristics. The most common approaches to designing this type of OWC come from laboratory experiments and numerical modelling. Usually, laboratory tests are more accurate, but they need adequate facilities and are more expensive to execute. On the other hand, numerical models need proper validation with collected data from experiments. Furthermore, depending on its fidelity, numerical models do not represent all the processes involved in the OWC chambers, such as sloshing and air compressibility. To narrow the uncertainty around multi-chamber OWC design and to improve its efficiency and knowledge, in the present work, a new methodology uses a combination of experimental and numerical approaches (both high-fidelity fast- and slow-CFD simulations) in the design process of such devices.

2.1. Objectives

The main objective of the methodology is to design multi-chamber OWCs quickly and accurately. These results permit understanding their behaviour at the prototype scale. The new methodology combines experimental and high-fidelity numerical modelling within the OpenFOAM environment (Weller et al., 1998).

The workflow of the methodology is presented in Fig. 1, and it assumes that a pre-design task has been made to define the scaled model OWC (top black box) using, for example, low-fidelity numerical modelling (Rezanejad et al., 2015). The green and orange boxes correspond to CFD simulations. The green boxes correspond to the PTO modelled with actual holes, and the orange boxes correspond to the PTO modelled with numerical damping regions. The last experimental tasks,

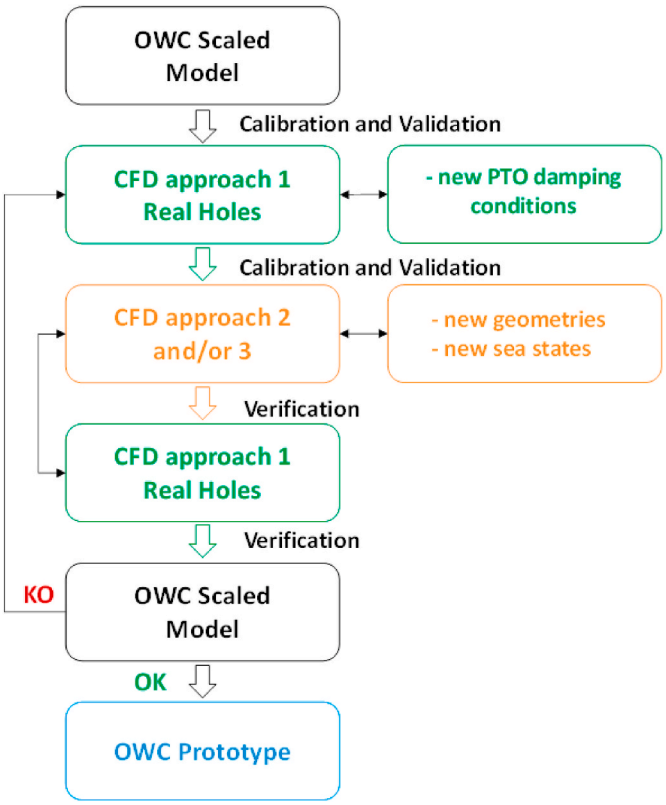

Fig. 1. Workflow diagram of the present methodology to design multi-chamber OWCs. Black colour corresponds to experimental work, green colour to CFD simulations with PTO modelled with approach 1 and orange colour to CFD simulations with PTO modelled with approaches 2 and 3.

both model and prototype scales, are represented with the bottom black and blue boxes, respectively.

To show the part of the CFD simulations methodology workflow, only the green and orange boxes are replicated in the present work and three approaches to model the PTO damping conditions are used. One approach physically represents the damping holes used in the experiments (Approach 1 - described in section 3.2.1), and two approaches use damping numerical regions: in the second approach the PTO is modelled as a porous media which induces a loss of momentum (Approach 2 - described in section 3.2.2), while in the third approach the PTO is modelled by a sink of momentum induced by a linear velocity damping term (Approach 3 - described in section 3.2.3). However, the present methodology can be used only with Approach 2, Approach 3 or an alternative faster approach to model the PTO damping conditions.

The advantages of using numerical damping regions (approaches 2 and 3) instead of using the real geometry of the holes (approach 1) are mostly connected to computational savings. Usually, numerical regions are larger in volume and are defined with bigger cells, which theoretically will speed up the simulations with fewer hardware requirements. Another strength of this methodology is that it saves time because it does not need to re-mesh all the cases for a different PTO damping. There is only the need to change the input parameters. For approach 1, a new geometry of the orifice must be defined, and the entire case must be re-meshed.

The first step in this methodology is to collect data from preliminary experimental tests in a scaled model represented in the top black box. This leads to the second step, where the experimental data is used to calibrate and validate the NWT with real holes (Approach 1) and numerical regions (Approach 2 and 3). Results from sections 4 and 5 will show that Approach 3 provides accurate and robust validation, with more computational efficiency than Approach 1 and 2.

The key to the present methodology relies on this iterative process between approach 1 and approaches 2 and 3. Once the NWT is calibrated and validated with real holes, the geometry of these holes can be changed within the numerical model, and the new results can be considered valid to calibrate and validate approaches 2 and 3, saving time by doing new experimental tests with new hole geometries. Basically, changes in approach 1 permit the study of new PTO damping conditions and calibrate and validate approaches 2 and 3. Faster CFD simulations with approaches 2 and 3 permit the study of new designs with varying geometries, sea states, and locations.

Once the numerical design of the model using approaches 2 or 3 reaches a satisfactory criterion, it is advised to test it again with approach one and subsequently test it in the laboratory before going to a full-scale prototype. If the new experimental tests confirm the numerical model premises, then, with the advisable considerations, it is possible to produce the full-scale prototype. On the other hand, if the new scaled model tests don't confirm the numerical model premises, then the collected data can be used as the new calibration results for the numerical model.

The downside of the present methodology is that the damping cannot be changed using numerical regions (approaches 2 and 3). These approaches are not able to describe the flow near the PTO because the geometry at the top lid is entirely different. Usually, the computed air velocities around the PTO are much smaller than in reality, and eventual second-order effects cannot be reproduced because they are not affected by flowing through a very narrow channel. Another limitation is that the constants that must be tuned in approaches 2 and 3 have no physical meaning and have no direct relation with the physical holes. As proposed before (Fig. 1), approaches 2 and 3 must be validated either with experimental data or numerical results from approach 1. In future, a relationship between these constants and the real PTO damping characteristics must be established.

2.2. Pneumatic efficiency assessment methodology

The pneumatic efficiency η_i for the ith chamber is the fraction of the mean power $\overline{P}_i$ absorbed compared to the mean incident wave power $\overline{P}_{inc.}$ and is expressed by the equation:

$$\eta_i = \frac{\overline{P}_i}{\overline{P}_{inc.}}, i = 1, 2, 3 \tag{1}$$

where $i = 1, 2, 3$ corresponds to the first, second or third chamber respectively. The mean power $\overline{P}_i$ is calculated with the expression:

$$\overline{P_i} = \frac{1}{t_{max}} \int_0^{t_{max}} P_i dt = \frac{1}{t_{max}} \int_0^{t_{max}} p_i Q_i dt, i = 1, 2, 3 \tag{2}$$

where t_{max} is maximum time of the records and P_i is the instantaneous rate of work, given by expression:

$$P_i = p_i . Q_i . \tag{3}$$

where, p_i is the instantaneous air pressure and it comes from the readings recorded inside each chamber. And Q_i is the air flow and is defined as:

$$Q_i = L_i b D_i^3 \left(\zeta_i^j\right), i = 1, 2, 3 \tag{4}$$

This approximation is possible due to the relatively small size of the chambers in the scaled model compared to a full-scale prototype that permit to neglect compressibility and humidity effects (Falcão and Henriques, 2014). L_i and b are the length and the width the chambers and $D_i^3\left(\zeta_i^j\right)$ is an approximation of the FSE velocity and is calculated with the expression:

$$D_i^3\left(\zeta_i^j\right)=\frac{-11\zeta_i^j+18\zeta_i^{j+1}-9\zeta_i^{j+2}+2\zeta_i^{j+3}}{6\Delta t}, i=1,2,3 \quad (5)$$

where ζ_i^j is the FSE inside each chamber at time t_j and Δt is the time step. The mean incident wave power $\overline{P}_{inc.}$ in Eq. (1) is determined using the incident wave spectrum $S(\omega)$:

$$\overline{P}_{inc.}=b\rho g\int_0^{+\infty} S(\omega)c_g(\omega)d\omega, \quad (6)$$

where g is gravity, ω is the angular frequency, ρ is the water density, and c_g is the group velocity, and is given by:

$$c_g=\frac{1}{2}\frac{\omega}{k}\left(1+\frac{2kh}{sin\,h\,sin\,h\,2kh}\right), \quad (7)$$

where h is the water depth, k is the wavenumber and it comes from the expression:

$$\omega^2=gk\,tan\,h\,tan\,h\,kh, \quad (8)$$

Finally, the global pneumatic efficiency is expressed as:

$$\eta=\sum_1^i \eta_i, i=1,2,3 \quad (9)$$

3. Numerical model

The main software used in the present work is OpenFOAM v2406 (Weller et al., 1998). The software is natively coupled with the IHFoam toolbox (Higuera et al., 2014a, 2014b; Romano et al., 2020), which permits modelling wave generation and absorption and describing the flow across porous layers.

3.1. Governing equations

The main governing equations used in the present study are the Reynolds Averaged Navier-Stokes (RANS) and VARANS. While the RANS equations describe the fluid behaviour for modelling the PTO as circular holes (section 3.2.1) and as a velocity damping (section 3.2.3), the VARANS equations describe the PTO as a porous layer (section 3.2.2). Subsequently, the three methods are described.

3.1.1. RANS equations

The Navier-Stokes equations, for an incompressible flow for a Newtonian fluid are described as follows:

$$\rho\left(\frac{\partial v}{\partial t}+v\cdot\nabla v\right)=-\nabla p+\mu\nabla^2 v+\rho g, \quad (10)$$

where g is gravity, ρ is the fluid density, μ is the dynamic viscosity, p is the pressure, v is the velocity, and ∇^2 is the Laplace operator. The continuity equation is:

$$\nabla\cdot v=0, \quad (11)$$

The FSE tracking method is based on the volume of fluid (VOF) and is described as:

$$\frac{\partial\alpha}{\partial t}+\nabla\cdot(\alpha v)=0 \quad (12)$$

where α is the ratio of the fluid in each cell.

3.1.2. VARANS equations

The VARANS equations describe the fluid behaviour inside a porous layer, that in this case, is modelled as a continuous media. To avoid the disadvantages of using a microscopic approach, in the present case a macroscopic approach was used by averaging the behaviour within the porous zone (Romano et al., 2020). The Forchheimer's formulation, (Forchheimer, 1901) is used to model the drag forces:

$$\frac{\partial \underline{u}_i}{\partial x_i\,n}=0 \quad (13)$$

$$(1+c)\frac{\partial\rho\underline{u}_i}{\partial t\,n}+\frac{\underline{u}_j\partial\rho\underline{u}_i}{n\partial x_j\,n}=-g_j x_j\frac{\partial\rho}{\partial x_i}-\frac{\partial p^*}{\partial x_i}-f_{\sigma i}-\frac{\partial}{\partial x_j}\mu_{eff}\left(\frac{\partial\rho\underline{u}_i}{\partial x_j\,n}+\frac{\partial\rho\underline{u}_j}{\partial x_i\,n}\right)\pm A\underline{u}_i - B|\underline{u}_i|\underline{u}_i \quad (14)$$

$$\frac{\partial\alpha}{\partial t}+\frac{\partial\underline{u}_i\alpha}{\partial x_i\,n}+\frac{\partial\underline{u}_{ic}\alpha(1-\alpha)}{\partial x_i\,n}=0 \quad (15)$$

Following (Gent, 1995), the Forchheimer equations can be expressed as:

$$A=a\frac{(1-n)^2\mu}{n^3D_{50}^2} \quad (16)$$

$$B=b\left(1+\frac{7.5}{KC}\right)\frac{(1-n)\rho}{n^3D_{50}} \quad (17)$$

$$C=\gamma\frac{1-n}{n} \quad (18)$$

where μ is the dynamic viscosity, u is the velocity, ρ density and p is the pressure. α and β are the linear and nonlinear friction coefficients, respectively. The porosity of the material is expressed as n, c is the added mass coefficient, D_{50} is the nominal diameter, and KC is the Keulegan-Carpenter number (Keulegan and Carpenter, 1958).

3.2. PTO modelling

The PTO damping in each chamber is modelled using three techniques, and their results are compared with experiments. As explained before, approach 1 is the geometry replication of the orifice used in the experimental trials. Approaches 2 and 3 use numerical regions to artificially dampen the flow in this area.

The numerical regions are defined with square areas 10x bigger than the equivalent orifice areas (Fig. 2). This permits the use of a coarser mesh in this region, leading to computational savings.

3.2.1. Approach 1 - PTO simulated with orifices

In the first approach, an orifice with the same dimensions used in the experiments is defined to simulate the PTO damping. To properly model the hole, an extra refinement of the mesh was done in its vicinity to guarantee at least four cells per diameter. This is visible in Fig. 3, which shows a comparison between the meshes used in the vicinity of the PTO

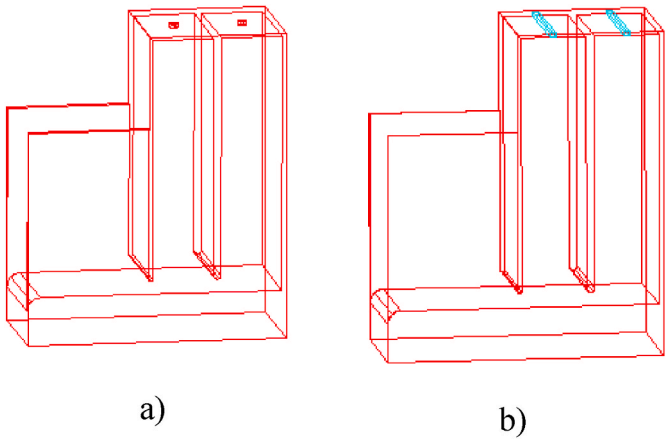

Fig. 2. PTO configurations for the DCOWC: a) PTO modelled with the geometry of the orifice; b) PTO modelled with numerical regions.

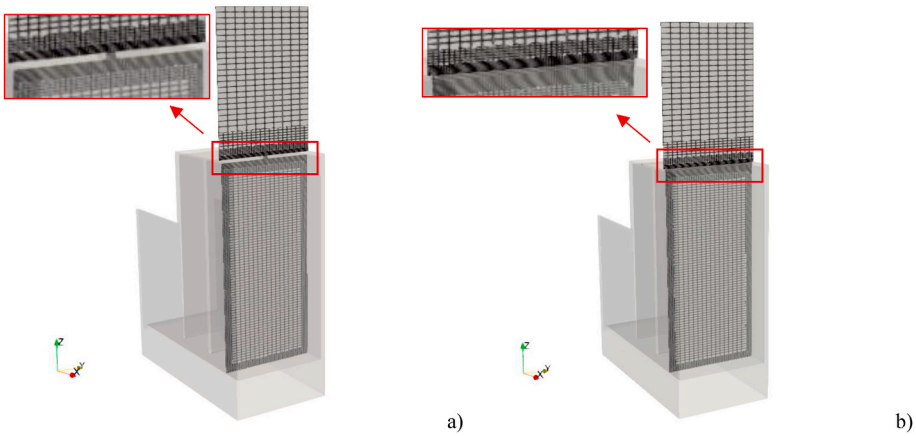

Fig. 3. Comparison of the mesh characteristics in the vicinity of the PTO: a) modelled as in the experiments (Approach 1); b) modelled as numerical regions (Approaches 2 and 3).

modelled with an orifice and numerical regions. The extra refinement permits a correct replication of the airflow.

3.2.2. Approach 2 - PTO simulated with porous layers

An innovative approach is applied to model the damping created by the PTO using a porous zone to overcome the complex interaction of the airflow through the holes using the VARANS equations. The complex geometry of the holes (Fig. 2a). is substituted by a porous media along the entire top of the chamber. (Fig. 2b). The comparison of the meshes is shown in Fig. 3.

Outside the numerical region, the porous media frictional forces are neglected (a = b = c = 0), and the porosity is defined as 1. This artifice substitutes VARANS equations with RANS equations. Inside the porous media, the full set of VARANS equations are solved. This means that the parameters a, b, c, D50, KC, and n from Eqs. (13)–(18) must be defined. This technique permits the model of the entrance and exit of the airflow in the porous zone, as well as the damping inside. This means that the resistance and reflection effects inside the porous media are reproduced, and part of the flow is reflected into the chamber.

3.2.3. Approach 3 - PTO simulated with velocity damping

Again, as for approach 2 (section 3.2.2), the same simplified geometry will characterise the PTO. In this case, the PTO is simulated with velocity damping, which is included directly in the momentum equation. This type of approximation is possible since the porosity of the element is very high, and, therefore, a drag force can be directly applied in the moment equation. A new term is added (F_{drag}) in the RANS equations as follows:

$$\frac{\partial u_i}{\partial x_i} = 0 \tag{19}$$

$$\frac{\partial \rho u_i}{\partial t} + \frac{u_j \partial \rho u_i}{\partial x_j} - \frac{\partial}{\partial x_j}\left(\mu_{eff}\frac{\partial \rho u_i}{\partial x_j}\right) = \frac{\partial p^*}{\partial x_i} - g_j x_j \frac{\partial \rho}{\partial x_j} - F_{drag} \tag{20}$$

$$F_{drag} = a\|U\| + b\|U\|^*\|U\| \tag{21}$$

where $\|U\|$ is the velocity and a, b are empirical coefficients with no physical meaning and need to be tuned in an iterative process by comparing the key physical quantities inside the chambers with results from experiments or approach 1 (real holes). In future, a relationship between these coefficients and the fundamental PTO damping characteristics must be established.

The entrance and exit of the air flow are not simulated, just a reduction inside the damping zone. This approach is much faster than using the VARANS equations, but on the other hand, it cannot correctly reproduce the effect of air flow entering a zone with low permeability. Compared to Approach 2 (section 3.2.3), this approach can reproduce the resistance component inside the porous media, but the reflection effects cannot be reproduced.

4. Model validation: DCOWC

The numerical wave tank (NWT) is validated with physical experiments from the campaign described in Gadelho et al. (2024b). The experimental set-up is described in section 4.1 and the numerical set-up is described in section 4.2. Calibration (section 4.3) and Validation (section 4.4) justify the assumptions and modelling used in this work.

4.1. Experimental set-up

The experimental campaign used to validate the present CFD numerical model was performed at the National Laboratory of Civil Engineering (LNEC), Portugal. The wave tank is 30.0 m long and has a variable cross-section that goes from 1.0 m upstream down to 0.6 m near the DCOWC. The bottom is also variable, with a water depth of 0.684 m near the wavemaker that reduces to 0.384 m near the DCOWC. Fig. 4 shows its peculiar geometry.

The geometrical scale of the experiments was 1/25. The DCOWC was positioned 25.0 m from the wavemaker. In this area, the wave flume has 0.06 m, which means that there exists a gap of 0.05 m between the model and the walls. A fully absorbing beach made with rocks was installed downstream of the flume. For more details of the experimental campaign and results consult Gadelho et al. (2024b).

4.2. Numerical wave tank

The Numerical Wave Tank's (NWT) geometry is based on the above-mentioned experimental campaign (section 4.1). After a calibration process performed in section 4.3, the NWT used in the simulations is 13.0 m long, 0.5 m wide, and 2.0 m high. The water depth is set to 0.384 m. The representation of the mesh and the entire domain is visible in Fig. 9a). The inlet of the NWT is defined as a patch (left side), where wave generation and active absorption are set. The outlet is defined as a wall (right side). The front and back patches are defined as walls with slip boundaries, and the bottom and top are defined as non-slip and open, respectively. The turbulence model used is the k-ω-SST model from Larsen and Fuhrman (2018).

The modelling of the present DCOWC is done using three different approaches, above mentioned, to model the PTO damping. Fig. 2a) represents the configuration used for approach 1 and in Fig. 2b), the configuration used in approaches 2 and 3. The dimensions of the model are represented in Fig. 5. In the experiments, an orifice (ϕ = 0.036 m)

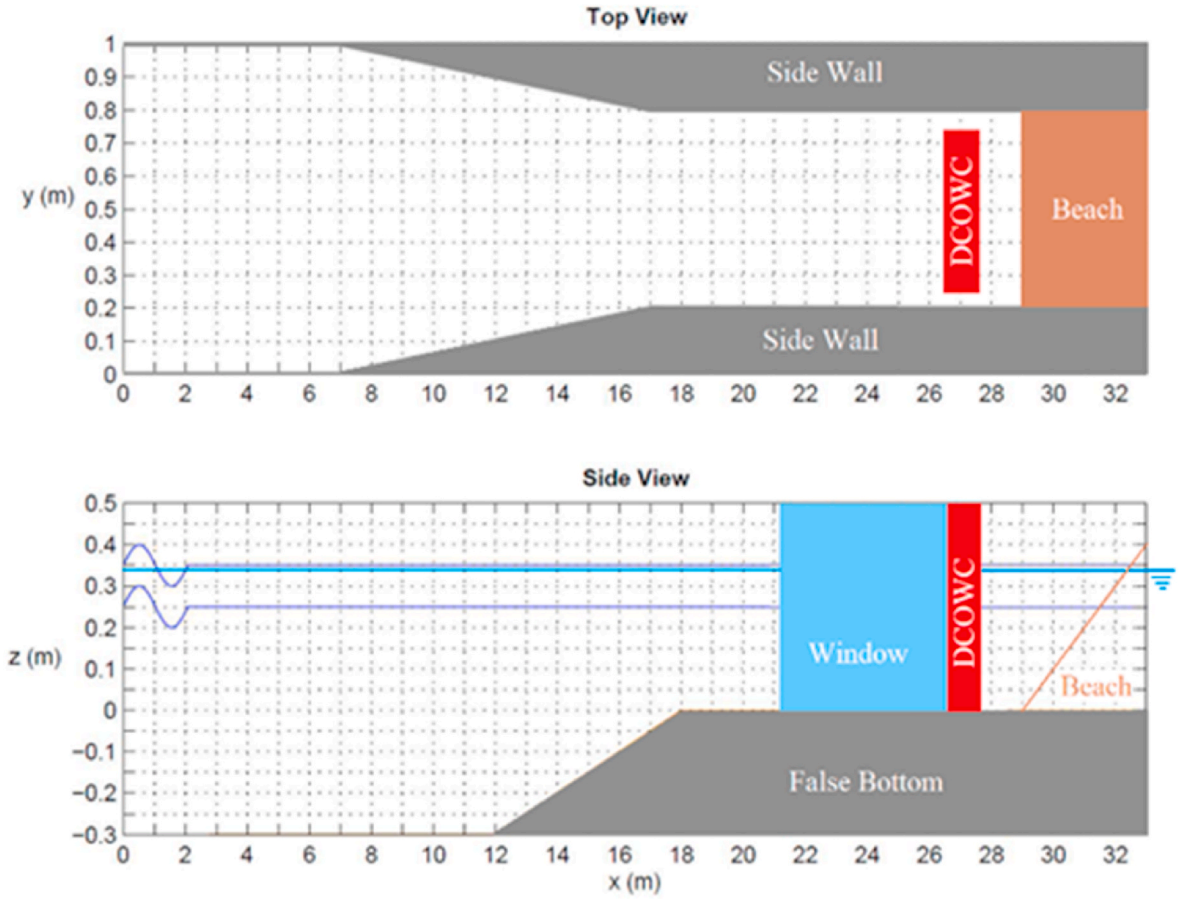

Fig. 4. COI3 wave flume geometry. Water depth near the DCOWC is h = 0.384 m. Not to scale.

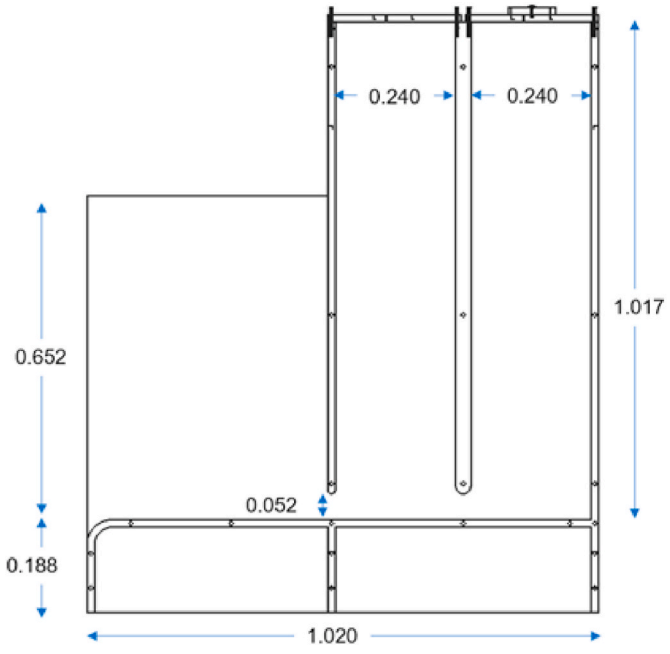

Fig. 5. DCOWC model with dimensions in m. The width is 0.5 m and the wall thickness is 0.015 m. The thickness between chambers is 0.030 m.

was used to model the PTO damping. Chamber 1 is located facing the incoming waves (left side), while Chamber 2 is located next to the beach side (right side).

The results of the Free Surface Elevations (FSE) amplitudes, air pressure amplitudes, and primary efficiency are presented. First, the TCOWC uses a lower PTO damping configuration using Approaches 1 and 3. Second, the TCOWC is tested for a scenario where the PTO damping is higher, where the circular hole areas are reduced by 60 %. Lastly, the present TCOWC results are compared to the DCOWC numerical results. Table 1 shows the list of cases with the PTO orifice dimensions.

A total of 89 simulations with regular waves (H = 0.04 m and T = 0.8 s–3.2 s) are performed. Table 2 presents a list of all the CFD simulations. CFD0 and CFD60 correspond to low and high PTO pneumatic damping conditions, respectively, and the grey cases are used in the calibration and validation process.

4.3. Calibration of the numerical wave tank

The model is calibrated for a DCOWC with the PTO modelling defined as orifices. Two sensitive analyses are made: one to define an efficient computational domain and another to define the mesh refinement. The numerical results are compared with experimental data for the case with H = 0.04 m and T = 2.0 s. More details about the experiments are presented in Gadelho et al. (2022). Two numerical set-ups with almost the same mesh resolution are used to evaluate the domain sensitivity. The first domain simulates the full dimensions of the

Table 1
List of the cases with the PTO orifice dimensions.

Case	% of orifice area reduction	ϕ (m)
CFD0	–	0.036
CFD60	60 %	0.020

Table 2
List of the CFD simulations. CFD0 and CFD60 correspond to low and high PTO damping conditions, respectively. Grey cases are used in the calibration and validation process. H = 0.04 m.

	CFD0					CFD60	
	DCOWC			TCOWC		DCOWC	TCOWC
T (s)	AP1	AP2	AP3	AP1	AP3	AP1	AP1
0.8	-	x	x	x	x	x	x
1.0	x	x	x	x	x	x	x
1.2	x	x	x	x	x	x	x
1.4	x	x	x	x	x	x	x
1.6	x	x	x	x	x	x	x
1.8	x	x	x	x	x	x	x
2.0	x	x	x	x	x	x	x
2.2	x	x	x	x	x	x	x
2.4	x	x	x	x	x	x	x
2.6	x	x	x	x	x	x	x
2.8	x	x	x	x	x	x	x
3.0	x	x	x	x	x	x	x
3.2	-	x	x	x	x	x	x

experimental wave flume. Fig. 6 shows a snapshot of the simulations, where it is visible that the gap between the model and the walls introduces little interference on the wave stream. The domain's length is 33.0 m and the width is 0.6 m. The mesh has around 3M cells. The second domain simulates the wave flume without a portion of the inlet, with a reduced length of 13.0 m, and its cross-section width is reduced to 0.5 m. The mesh is around 0.8M cells. This permits the elimination of the gap, leading to the avoidance of non-desirable numerical 3D effects and gains in terms of computational efficiency.

Globally, the second domain (cut domain) is more accurate and faster to simulate than the first (Gadelho et al., 2022). The final numerical mesh for the first domain (3M cells) runs for 4.5 days in 10 HPC (High-Performance Computing) cluster processors. The second domain (0.8M cells) run for 2.5 days in 4 processors of a regular desktop.

The mesh refinement sensitive analysis was made by comparing the FSE envelopes, and the key physical quantities inside both chambers, between 3 meshes for the case with regular waves H = 0.02 m and T = 2.0 s and for the cut domain. The mesh details are presented in Table 3, and all of them run for 40 s. The refinement is made from the course Mesh0 to the more refined Mesh2 multiplied by a factor in the x and z directions.

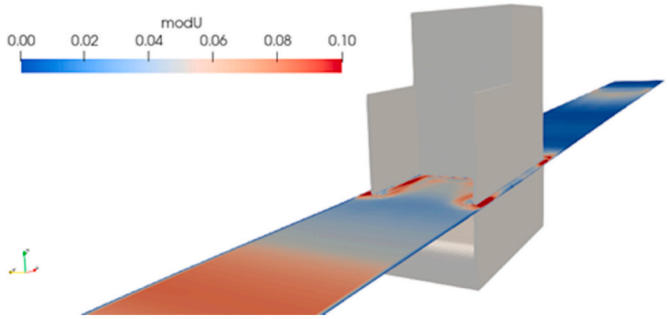

Fig. 6. Example of the NWT simulated for the whole computational domain.

Results of the FSE envelope are shown in Fig. 7. In this case, the envelope is defined as the maximum and minimum free surface elevation recorded at a given x coordinate of the wave flume for 40 s of simulation. It is visible the presence of nodes and anti-nodes, and this is a clear indication of wave reflection from the OWC. The key physical quantities inside time series inside both chambers are represented in Fig. 8.

From these 2 figures, it is possible to say that all three meshes can reproduce virtually the same results. When comparing the computational costs, Mesh0 (0.47M cells) ran for 3 days using 1 CPU, Mesh1 (0.8M cells) ran for 4 days using 4 CPUs, and Mesh2 (1.4M cells) ran for 6 days using 8 CPUs of a regular desktop.

With obvious efficiency advantages and virtually giving the same results, the reduced numerical domain and the coarser mesh were used for the rest of the simulations. The final mesh has a cell resolution of 0.06 m, 0.05 m and 0.025 m along the x, y and z directions, respectively. A local refinement around the FSE was made to track accurately the wave propagation (dx = 0.03 m, dy = 0.025 m, and dz = 0.125 m). To model the PTO with approach 1, an extra refinement around the orifice was made to guarantee a proper airflow (dx = 0.0075 m, dy = 0.00625

Table 3
Mesh sensitivity analysis characteristics.

Mesh	Multiplication Factor	cells
Mesh0	1	0.47 M
Mesh1	$\sqrt{2}$	0.8 M
Mesh2	2	1.4 M

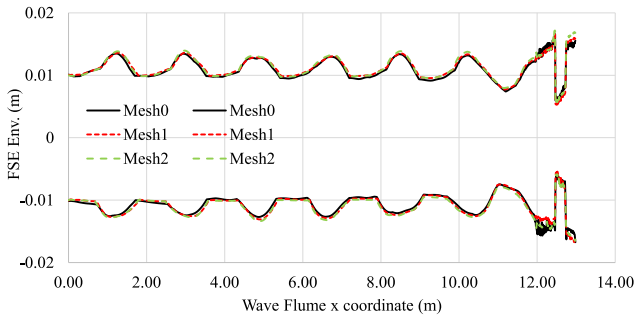

Fig. 7. Free Surface Elevation Envelope over the entire x domain of the tank for the 3 meshes.

m, and dz = 0.003125 m). Fig. 9 represents the NWT used in the simulations: a) Full domain; b) Portion of the mesh showing the refinement around the initial FSE and DCOWC.

4.4. Validation

The present CFD model's validation process consisted of comparing the results of the three PTO damping approaches with experimental data for the DCOWC. The first approach compared the air pressures inside the DCOWC with the experiments. Secondly, the FSE amplitudes, air pressure amplitudes and pneumatic efficiency are determined and compared for other wave periods. The two regular wave cases used to compare the air pressure time series are.

- w1: H = 0.035 m and T = 2.0 s
- w2: H = 0.039 m and T = 2.6 s.

For the PTO modelling approach 2, after an iterative calibration process, the constants used in Eqs. (16)–(18) are listed in Table 4.

The values used in this work for the PTO modelling approach 3 are a = 5000 and b = 10 000 (Eq. (21)). For the PTO modelling approach 1, no value needs to be calibrated.

The computational costs for the mesh with PTO modelling approach 1 (0.8M cells), took 4 days to simulate 40 s in 4 processors of an HPC cluster. For PTO modelling approaches 2 and 3 (0.5M cells), the simulations took 3 days and 2.5 days, respectively, using 2 processors of a

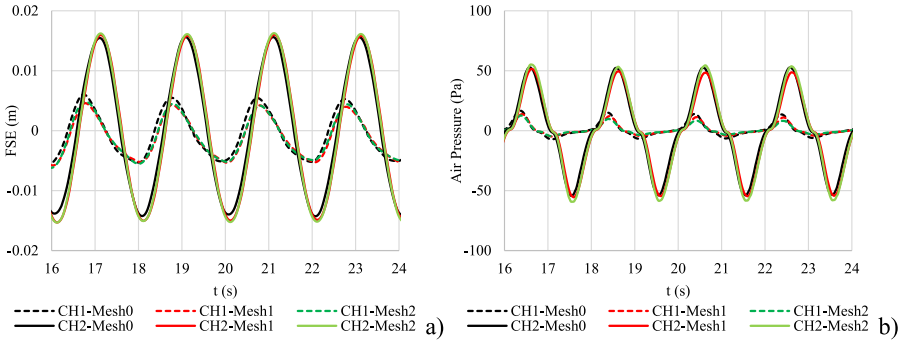

Fig. 8. Key physical quantities time series inside the chambers for the mesh sensitive analysis: a) Air pressures and b) Free Surface Elevations.

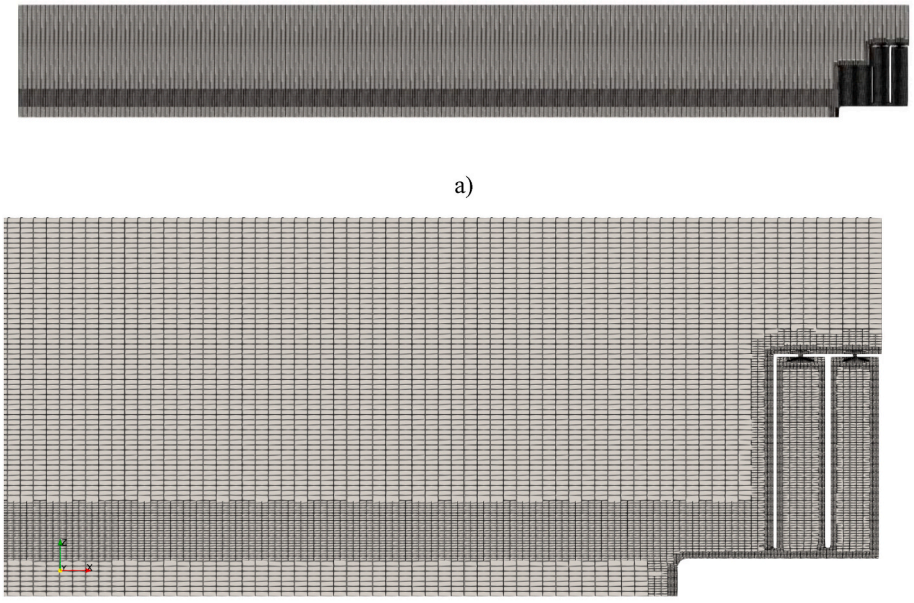

Fig. 9. Representation of the NWT used in the simulations: a) Full domain; b) Portion of the mesh showing the refinement around the initial FSE and DCOWC.

Table 4
Approach 2 constant values.

Constant	value
A	2
b	2
c	0.34
D_{50}	0.0159
porosity	0.25

regular desktop.

Fig. 10 shows the air pressures inside the chambers for w1. It shows in Fig. 10a) that in chamber 1, the amplitude that has the most similar magnitude compared to the experiments is the one that models the PTO with porous media (Approach 2). All approaches cannot replicate the air pressure entirely over time. For chamber 2, Fig. 10b), the results compare much better, and all the PTO modelling techniques present good results.

Fig. 11 shows the air pressure inside the chambers for w2. The CFD results of the three approaches for chamber 1, Fig. 11a) show that the air pressure curve is identical between them but cannot accurately reproduce the experimental results. All models overpredict the maximum air pressure. For the first chamber, approach 2 seems to reproduce the air pressure better, especially in the negative part of the signal. For the second chamber, Fig. 11b), all the approaches cannot replicate the experimental air pressure curve and overpredict its positive and negative peaks. For more details, please consult Gadelho et al. (2022).

The second part of the validation consists of expanding the range of the wave periods that now range from 0.8 s up to 3.2 s and calculating the amplitudes of the FSE and air pressures inside both chambers and their partial and total pneumatic efficiencies. To do this, the FSE and air pressure time series are normalised. After the system reaches a steady state, the results of 10–20 waves are studied statistically, and their amplitudes are calculated. The primary efficiency is calculated according to section 2.2.

Fig. 12 represents the FSE amplitudes inside both chambers, as the numerical model describes, compared with the experiments. Results

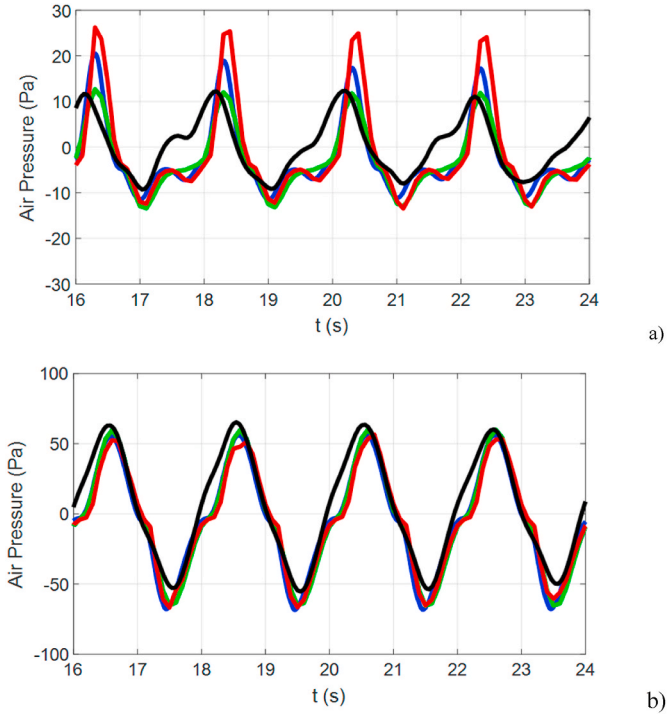

Fig. 10. Air pressures time series for w1: a) CH1; b) CH2. Black: Experiments; Blue: Approach 1; Green: Approach 2; Red: Approach 3.

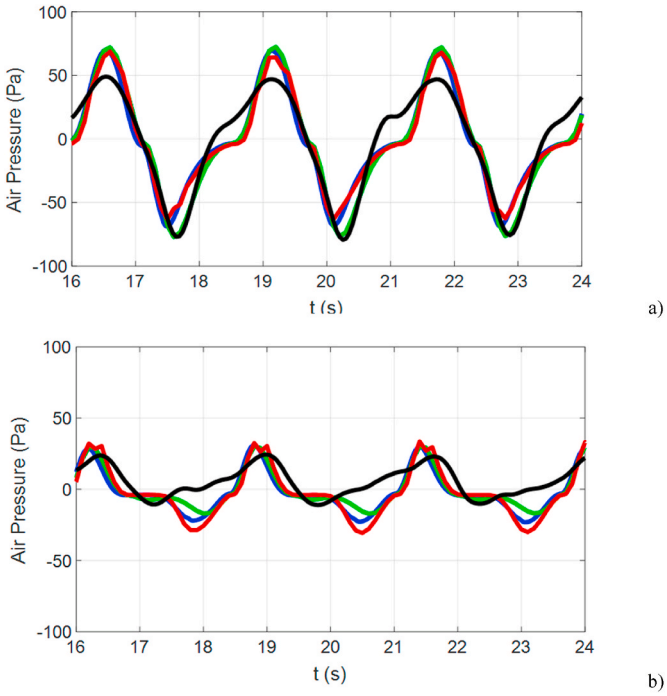

Fig. 11. Air pressures time series for w2: a) CH1; b) CH2. Black: Experiments; Blue: Approach 1; Green: Approach 2; Red: Approach 3.

show that, generally, all approaches can reproduce the shape of the FSE amplitudes for both chambers. For chamber 1, all three approaches fail to accurately reproduce the local peak values obtained in experiments, T = 1.2 s and T = 2.0 s. This might be connected to the inability of the numerical model to reproduce all phenomena observed in the experiments, namely persistent sloshing. For chamber 2, where the results are "smoother", for higher periods. all approaches overpredict the FSE, with approach 2 being the worst in this scenario.

In Fig. 13 the air pressure amplitudes inside both chambers are represented. Again, all approaches can reproduce the shape of the curve of the air pressures. However, there are two situations where the numerical model does not accurately reproduce the experiments.

The first is in chamber 1, for T = 1.2 s where all approaches do not reproduce the local peak. This might be connected to resonance effects between the experiments' chambers, which the numerical model cannot reproduce. The other is in chamber 2, for T = 3.2 s, where an evident drop in the experimental air pressure amplitude is visible, and the numerical model does not follow. Such a difference is hard to explain but might be connected to probable bad readings of the air pressure sensor in the experiments, for this case.

By dividing the FSE with the incident FSE amplitude, Fig. 14 is obtained. This figure is similar to Fig. 12 but now an evident amplification of the FSE in Chamber 2 is visible. The FSE can go up to 1.4x the incident FSE amplitude in the experiments. In the numerical model, this value is overpredicted, and the amplification can go up to 1.8x for approach 2. This is an indication that the CFD model can replicate the main interactions of the water exchange between chambers but might fail to reproduce some dissipation processes.

Fig. 15 represents the DCOWC's total pneumatic efficiency. Results show that the three numerical approaches follow the curve's shape of the primary efficiency calculated in the experiments but fail to reproduce the peak efficiency of 0.4, visible at T = 1.2 s, underestimating this value to approximately 0.3.

As observed in the air pressure amplitudes, this difference can be connected to resonance effects between chambers present in the experiments that the numerical model cannot reproduce. There is also another period where there exists a significant discrepancy between

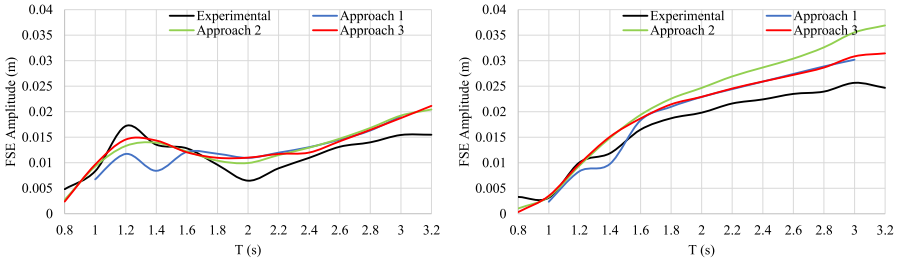

a) Chamber 1 b) Chamber 2

Fig. 12. FSE amplitudes inside both chambers.

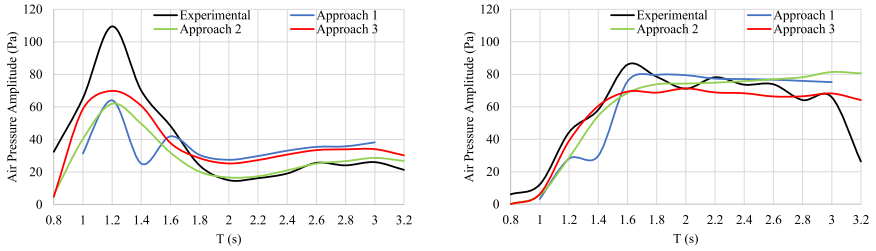

a) Chamber 1 b) Chamber 2

Fig. 13. Air pressure amplitudes inside both chambers.

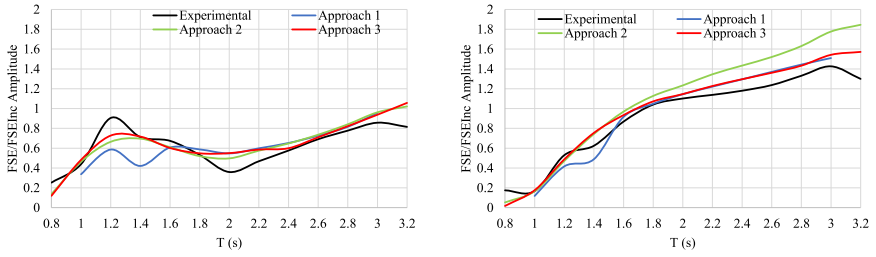

a) Chamber 1 b) Chamber 2

Fig. 14. Evolution of the FSE/Incident FSE amplitude inside the chambers.

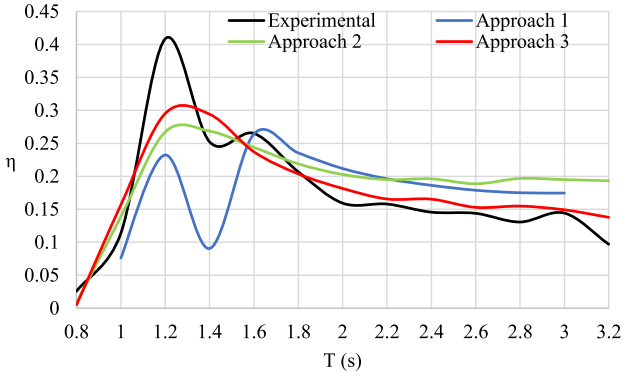

Fig. 15. Total DCOWC pneumatic efficiency for the experiments versus the three approaches.

results. At T = 1.4 s, the experimental results show a local minimum that approaches 2 and 3 fail to reproduce. On the other hand, approach 1 shows this local minimum but severely underestimates this value. This second-order effect might be connected to the airflow inside the chambers, but it might have no physical meaning in the Approach 1 numerical model. As expected, the air flow is much different from approach 1 to approaches 2 and 3, due to the completely unrealistic flow in the vicinity of the PTO described by these last two approaches.

The damping artifice reduces the air velocities in the hole by 10x for the last two approaches. This means that modelling the PTO with real holes (Approach 1) can reproduce this second-order effect, but its magnitude might not be well reproduced. This second-order effect should be investigated in detail.

The primary efficiency results for each chamber are presented in Fig. 16. Results show that all the numerical approaches can estimate effectively that chamber 1 is more efficient for lower periods while chamber 2 is more efficient for higher periods. The most significant differences are connected to chamber 1, where the three approaches fail to reproduce the peak efficiency of 0.35, estimating a much lower value, around 0.2. For the same chamber, approach 1 presents a big drop in the

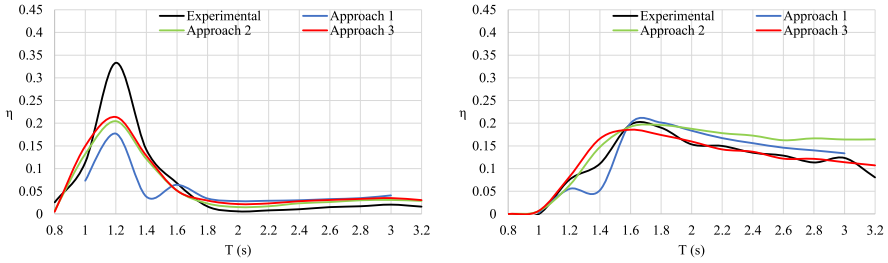

Fig. 16. Primary efficiency of the DCOWC: a) Chamber 1; b) Chamber 2.

efficiency at T = 1.4 s. As explained before, it might be connected to a second-order effect provoked by the airflow inside the chamber. The results for chamber 2 show a better agreement.

Appendix A presents the free surface and the flow velocities near the chamber for the DCOWC with the PTO modelled with approach 1. Appendix B and Appendix C show the same results but with the PTO modelled with approaches 2 and 3, respectively.

5. Efficiency of a triple-chamber OWC

5.1. Triple-chamber OWC

In this section, a numerical study with a new configuration of a multi-chamber OWC with three chambers, that could not be tested experimentally, is presented. This new configuration permits to fully validate the use of numerical regions to model the PTO (approach 3) compared to the use of real holes (approach 1). In this case, only approach 3 was used because it is faster than approach 2 and presents similar results. As explained before, the use of approach 2 is only useful if it is necessary to model the peculiarities of the effect of air flow entering a zone with low permeability, such as the use of damping material in the experiments. Compared to approach 2 this approach can reproduce the resistance component inside the porous media, but the reflection effects cannot be reproduced.

The geometry of the TCOWC is a simple extension of the DCOWC, which is just adding a third chamber of equal dimensions. Its dimensions are shown in Fig. 17. Once a good agreement of the results was obtained for the DCOWC between the numerical and experimental models in the previous section, the present TCOWC numerical model can be considered validated, and the results are reliable. However, experimental work should be developed to confirm the present results.

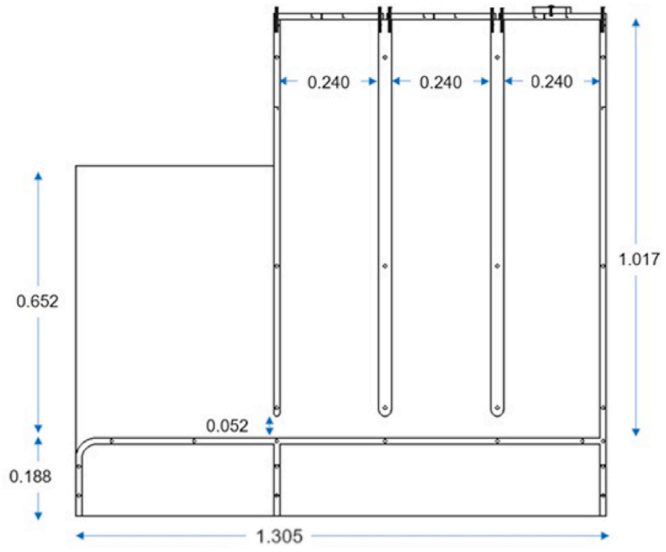

Fig. 17. TCOWC model with dimensions in m. The width is 0.5 m. The wall thickness is 0.015 m. The wall thickness between the chambers is 0.030 m.

5.2. Numerical wave tank

The numerical domain is discretised as in section 4.3. The initial cell resolution is 0.06 m, 0.05 m and 0.025 m along the x, y and z directions, respectively. An extra refinement was applied near the FSE where the cell dimensions are half of the initial size (dx = 0.03, dy = 0.025, and dz = 0.125).

For the modelling of the PTO with approach 1 (Fig. 18a), cell size around the holes is refined to obtain a final resolution of dx = 0.0075m, dy = 0.00625m, and dz = 0.003125m. For modelling the PTO with approaches 2 and 3 (Fig. 18b), cell size around and inside the porous zone is refined to obtain a final resolution of dx = 0.0075m, dy = 0.00625m, and dz = 0.003125m. Therefore, for approach one, the final mesh has 1.0 M cells, and for approaches 2 and 3, the final mesh has 0.6M cells.

The NWT is shown in Fig. 19 and is 13.27m long, 0.5m wide, and 2m high. The water depth is 0.384m. Regarding computational costs, simulations with the PTO modelling approach 1 (1.0M cells) took 4 days to simulate the 60s numerically, using 4 CPUs of an HPC cluster. Simulations with the PTO modelling approach 3 (0.6M cells) took 3 days to simulate the 40s numerically, using 2 CPUs of a regular desktop. In this case, it is evident that by expanding the DCOWC to a TCOWC, the gains in terms of CPU time using approach three instead of approach one is even more significant. Because the scalability of the problem is not linear and the hardware characteristics are completely different between PTO modelling approaches, it is safe to say that the gains in CPU time are around 60 % when using Approach 3 instead of Approach 1. The maximum y + values around the TCOWC are less than 300 for all the simulations.

5.3. Results

5.3.1. Triple-chamber CFD0 – approaches 1 and 3

Both NWT Approaches 1 and 3, have the same dimensions, with the only difference being the definition of the PTO. The numerical region is defined as a square 10 times bigger than the corresponding holes. Fig. 20 shows the FSE amplitudes inside the three chambers for both approaches, 1 and 3. Results show that the two methods are similar for all the range of wave periods, but Approach 3 always shows a slight underprediction of this quantity. It is interesting to observe that chamber 1 shows higher FSE amplitudes for lower periods, and chamber 3 shows higher FSE amplitudes for higher periods. The middle chamber always has lower or intermediate FSE amplitudes.

Fig. 21 represents the air pressure amplitudes inside the three chambers. They show that the results of both approaches are similar. Like the FSE amplitudes, the air pressures are higher in chamber 1 in

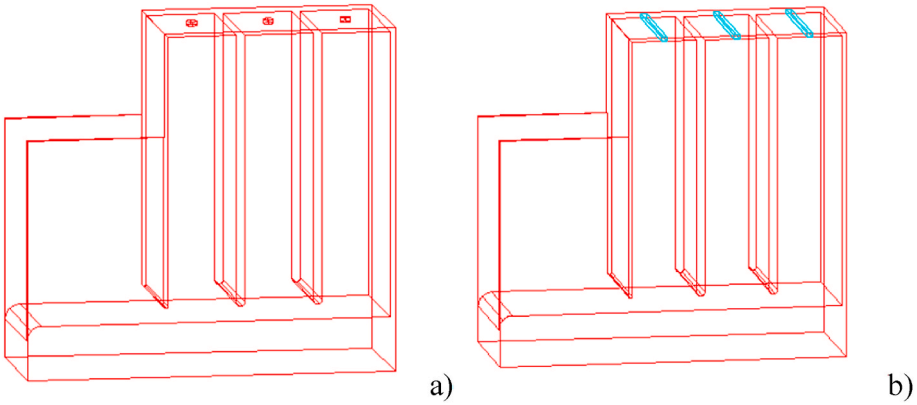

Fig. 18. TCOWC model: a) PTO modelled with orifices; b) PTO modelled with numerical regions.

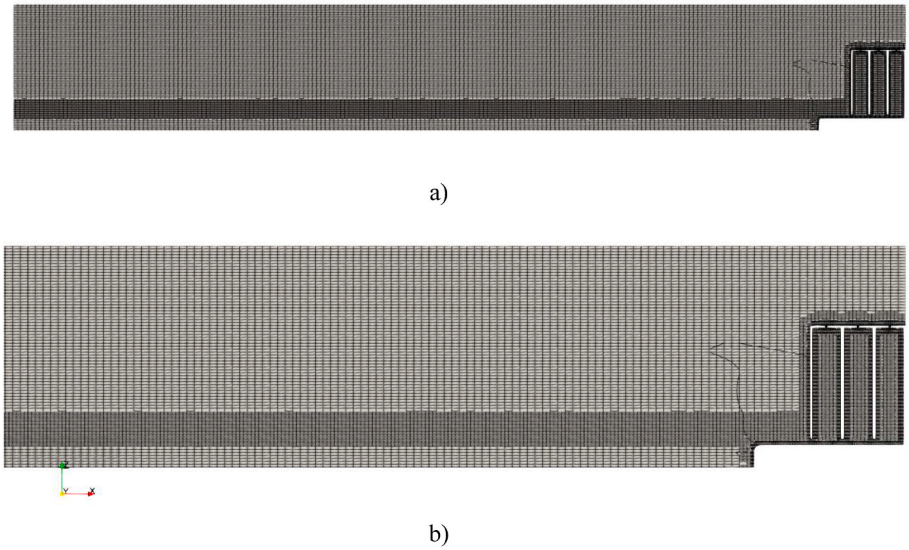

Fig. 19. Representation of the NWT used in the simulations: a) Full domain; b) Portion of the mesh showing the refinement around the initial FSE and TCOWC.

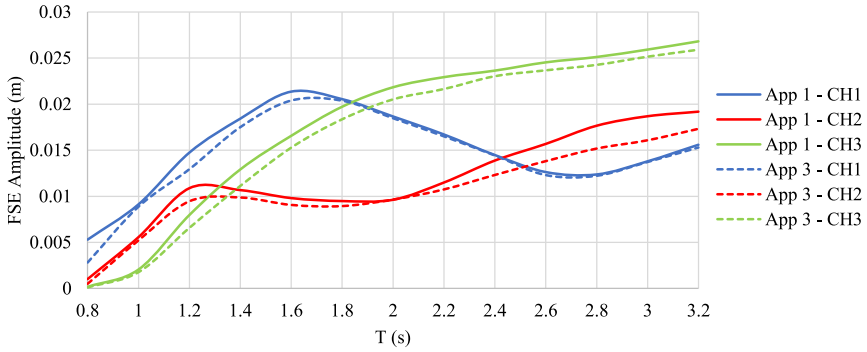

Fig. 20. Free Surface Elevation Amplitudes inside the chambers.

lower periods. For higher periods, chamber 3 records higher air pressures. The middle chamber always has lower or intermediate air pressure amplitudes.

Fig. 22 shows the pneumatic efficiency of the TCOWC. Results have a similar trend between approaches in all chambers. The biggest difference in the efficiency calculation is for the range of T = 1.2 s to T = 1.6 s, where Approach 3 underpredicts the total primary efficiency compared to Approach 1.

This results from the underprediction of the peak efficiency in chambers 1 and 2. Another interesting observation is that the middle chamber presents almost no efficiency all over the wave period range, only a small peak efficiency for a narrow range.

The previous results of the DCOWC pneumatic efficiency for the experiments versus the three previous CFD approaches are presented in Fig. 15. Several considerations can be drawn by comparing these results with the present TCOWC total primary efficiency results. Both cases,

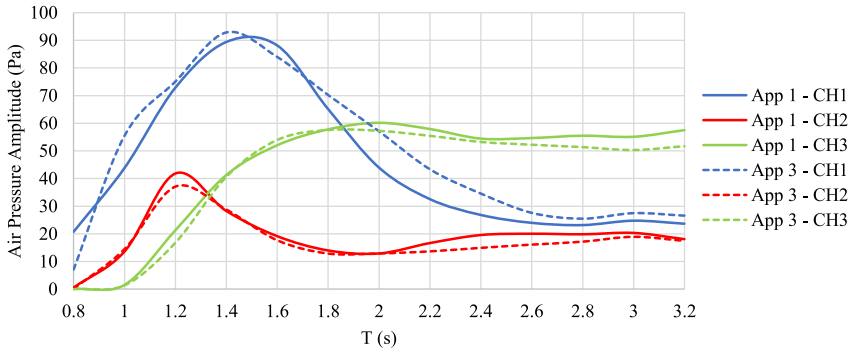

Fig. 21. Air Pressure Amplitude inside the chambers, CFD0, Approaches 1 and 3.

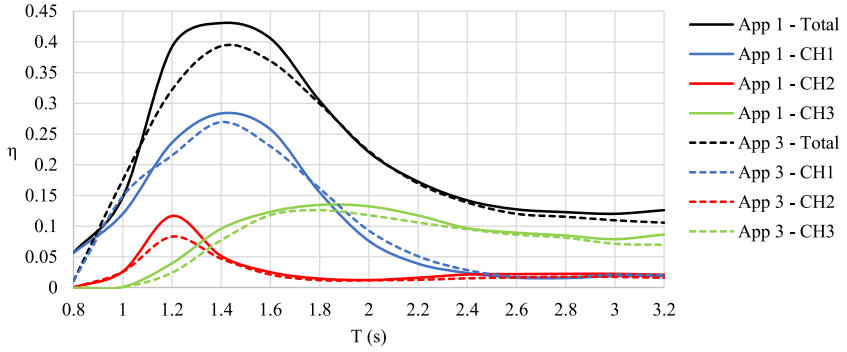

Fig. 22. Pneumatic efficiency of the TCOWC CFD0 – Approach 1 and 3.

DCOWC and TCOWC, have the same PTO damping configuration. The first observation is that the maximum primary efficiency recorded is 0.43 for the TCOWC at T = 1.4 s, while for the DCOWC, this value is around 0.4 in the experiments for T = 1.2 s (being only 0.3 in the CFD calculations). After T = 2.0 s, both devices present almost the same trend, reducing their efficiency to a range of 0.15–0.20 at T = 3.2 s. This means that, for this damping condition, the inclusion of a third chamber with similar dimensions has neglectable efficiency advantages, with the middle chamber performing poorly in almost all the tested wave period ranges. A more detailed discussion can be found in Appendix D where snapshots of the air velocity, FSE and vorticity for a wave cycle are shown.

5.3.2. *Triple-chamber CFD60 – approach 1*

Considering that CFD60 significantly improved the primary efficiency of the DCOWC device, the present CFD study is extended for the TCOWC device with this PTO damping condition using Approach 1. Fig. 23 represents the FSE amplitudes inside the TCOWC chambers for CFD0 vs CFD60. It is visible that, with the increase of the PTO damping conditions, the variations along the wave periods become much smaller. Generally, the FSE amplitudes are smaller for higher damping conditions. It is also observed that the FSE amplitudes increase almost linearly with the wave period for the CFD60.

Fig. 24 presents the TCOWC's air pressure amplitudes for both damping conditions, CFD0 and CFD60. Results show that increasing the damping conditions on all chambers increases their air pressures. As observed for CFD0, chambers 1 and 3 register higher air pressures for lower and higher wave periods, respectively. The middle chamber (chamber 2) always presents lower or intermediate air pressure amplitudes.

Fig. 25 compares the TCOWC efficiency for both PTO damping conditions, CFD0 and CFD60. It is observed that increasing the PTO damping (CFD60) dramatically increases the primary efficiency for periods higher than T = 1.6 s, from the lower 0.15 to a more significant

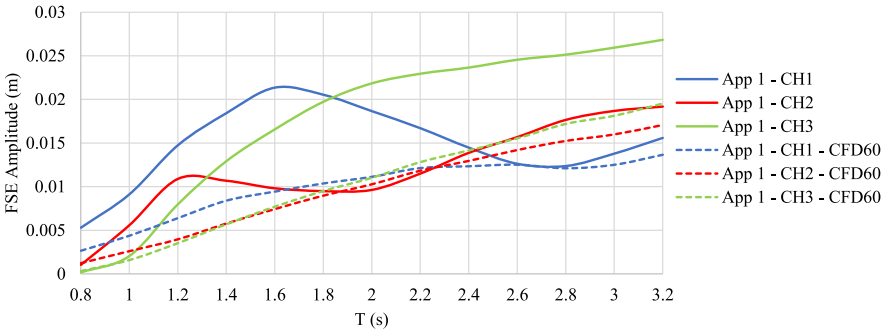

Fig. 23. TCOWC FSE amplitudes for CFD0 vs CFD60.

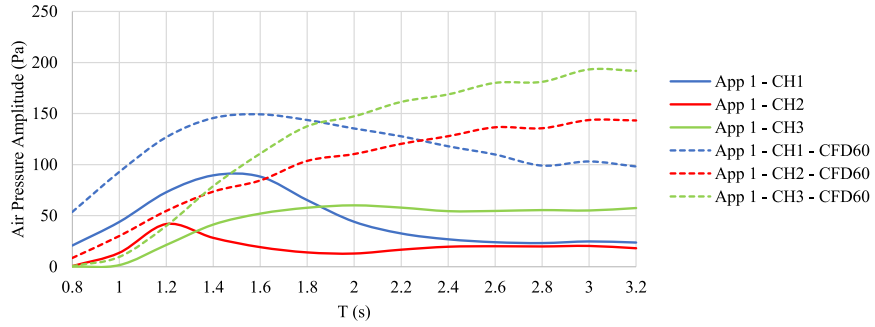

Fig. 24. TCOWC air pressure amplitudes for CFD0 vs CFD60.

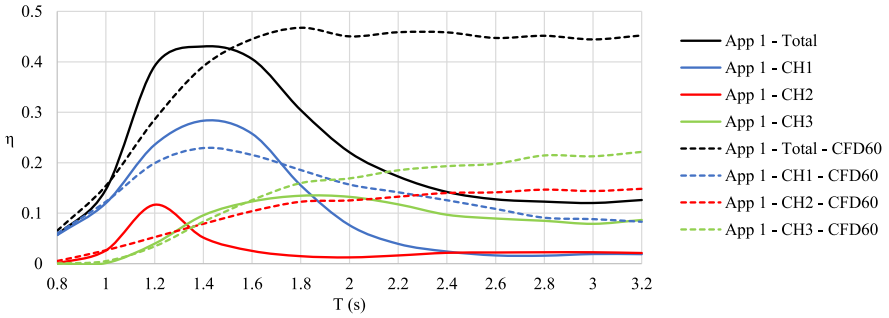

Fig. 25. Efficiency of the TCOWC for CFD0 vs CFD60.

0.45. After period T = 1.8 s, all chambers perform better for the higher damping condition. For lower periods, less than T = 1.6 s, the lower damping condition shows marginal advantages over the higher damping condition.

However, as with the DCOWC device, these results should be considered cautiously. The present primary efficiency results might be overpredicted due to probable air-compressible effects inside the chambers that are neglected in the numerical model. This spring-like air compressibility effect negatively impacts the primary efficiency estimation of OWCs and worsens when going for a full-scale prototype. A more detailed discussion can be found in Falcão and Henriques (2019). Although, generally, the curve of the primary efficiency shows a global improvement with the increase of the damping condition for higher wave periods.

5.3.3. OWC: 2 chambers vs 3 chambers CFD60 – approach 1

This subsection compares the OWC device with two chambers and the triple-chamber device for the higher PTO damping condition CFD60. Fig. 26 presents the FSE amplitudes inside the chambers for the DCOWC and TCOWC devices. Results show that, generally, the FSE amplitudes increase with the wave period in all chambers for both devices. The exception is chamber 1 in the TCOWC, where at T = 2.2 s, a constant value of around 0.012 m is assumed.

In Fig. 27, the results of air pressure amplitudes inside the chambers for the DCOWC and TCOWC devices are presented. They show that the DCOWC always presents higher air pressure amplitudes for periods higher than T = 1.4 s, presenting values as high as 280 Pa, while in the TCOWC, the highest air pressure amplitude record is less than 200 Pa in chamber 3. This means that including the third chamber balances the air pressure amplitudes recorded inside the chambers, thus protecting even more eventual PTO air pressure peaks.

The comparison of the primary efficiency between the DCOWC and TCOWC devices for CFD60 is presented in Fig. 28. The first and obvious conclusion is that the DCOWC total primary efficiency is higher periods higher than T = 1.2 s, assuming 0.6 after T = 1.8 s. The total primary efficiency of the TCOWC assumes a similar shape, but its maximum value is around 0.45. This means that including the third chamber might not benefit the primary efficiency in higher periods due to eventual

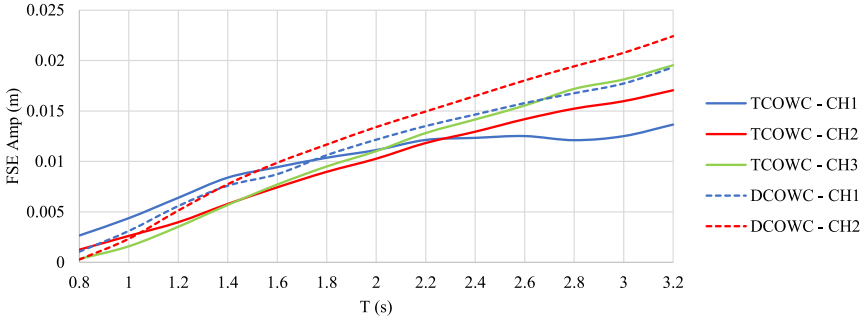

Fig. 26. FSE amplitudes inside the chambers for the DCOWC and TCOWC devices.

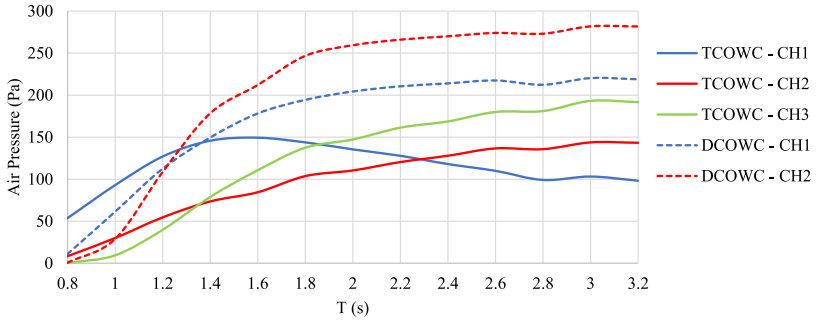

Fig. 27. Air pressure amplitudes for the DCOWC and TCOWC devices.

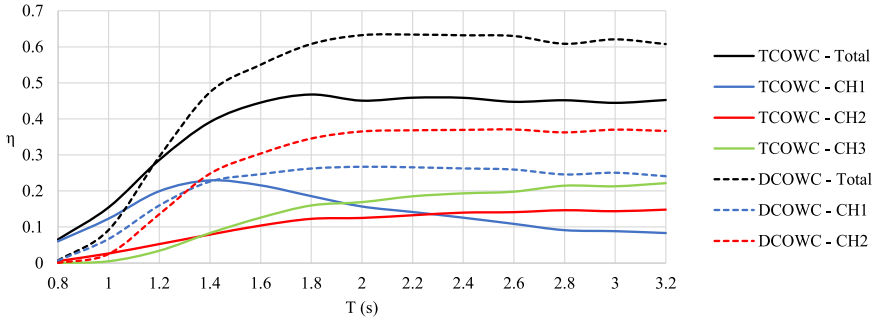

Fig. 28. Primary efficiency of the DCOWC and TCOWC devices.

dissipation processes while exchanging the water flow between chambers. Another evident conclusion is that for this PTO damping configuration, the middle chamber on the TCOWC continues to present low efficiency in all wave period ranges.

Appendix D presents snapshots of the FSE and vertical velocity of a TCOWC wave cycle with low PTO damping.

6. Conclusions

The methodology to estimate the primary efficiency of the TCOWC proved to work if the damping numerical regions of Approach 3 (60 % faster) are well calibrated with Approach 1 and experimental results from the DCOWC case. Results show that both approaches have identical physical quantities inside the chambers and the same primary efficiency trend.

Results also show that adding a third chamber has neglectable efficiency advantages compared to the dual-chamber OWC for the lower PTO damping condition CFD0. The middle chamber performs poorly in almost all the tested wave period ranges. By increasing the PTO damping (CFD60), the total primary efficiency of the TCOWC increases dramatically from 0.15 to a more significant 0.45 for higher wave periods, but still below 0.60 of the DCOWC. For lower wave periods, less than T = 1.6 s, the lower damping condition shows marginal advantages over the higher damping condition. For this PTO damping condition, the middle chamber on the TCOWC continues to present low efficiency in all wave period ranges.

However, these absolute results should be seen with caution, although the relative values should be relevant. The present primary efficiency results might be overpredicted due to probable air compressibility effects inside the chambers that are neglected in the numerical model. This spring-like air compressibility effect negatively impacts the primary efficiency estimation of OWCs and worsens when going for a full-scale prototype. A more detailed discussion can be found in Falcão and Henriques (2019). In future, simulations considering air compressibility should be done to assess its impact.

Overall, the methodology proved to be accurate, and the advantages of using damping numerical regions (Approaches 2 and 3) instead of using the real geometry of the holes (Approach 1) are evident in CPU savings. The downside of the present methodology is the fact that the numerical regions (approaches 2 and 3) cannot replicate the flow in the vicinity of the PTO, and the constants that must be tuned in approaches 2 and 3 have no physical meaning and have no direct relation with the physical holes. Approaches 2 and 3 must be validated with experimental data or numerical results from Approach 1. In future, a relationship between these constants and the fundamental PTO damping characteristics must be established.

CRediT authorship contribution statement

J.F.M. Gadelho: Writing – original draft, Visualization, Validation, Formal analysis. **G. Barajas:** Writing – original draft, Formal analysis. **J. L. Lara:** Writing – review & editing. **C. Guedes Soares:** Writing – review & editing, Supervision, Resources, Funding acquisition.

Declaration of competing interest

The authors declare that they have no known competing financial interests or personal relationships that could have appeared to influence the work reported in this paper.

Acknowledgements

The first author has been funded by the University of Lisbon, and CENTEC within a PhD grant.

The paper is done within the project “Harbour protection with dual chamber oscillating water column devices”, (HARBOUR OWC), which is co-funded by the European Regional Development Fund (Fundo Europeu de Desenvolvimento Regional - FEDER) and by the Portuguese Foundation for Science and Technology (Fundação para a Ciência e a Tecnologia - FCT) under contract PTDC/EME-REN/30866/2017.

This work contributes to the Strategic Research Plan of the Centre for Marine Technology and Ocean Engineering (CENTEC), which is financed by the Portuguese Foundation for Science and Technology (Fundação para a Ciência e Tecnologia - FCT) under contract UIDB/UIDP/00134/2020.

This work was produced with the support of INCD (Portuguese National Distributed Computing Infrastructure) funded by FCT and FEDER under the project 01/SAICT/2016 nº 022153.

APPENDIX-A. DCOWC WITH THE PTO MODELLED WITH APPROACH 1

Appendix A presents results (t = 40 s) for the DCOWC, PTO modelled with approach 1 (circular holes), cases with H = 0.04 m and T = [1.0, 1.4, 2.0, 2.6, 3.0] s, respectively. The top panel is complete NWT, with fluid velocities displayed in red-blue and air velocities in white-black. The bottom left panel has a free-surface elevation in light-dark green colours, and the right panel has a zoom in the vicinity of the dual-chamber OWC, with fluid velocities displayed in red-blue colours and air velocities in white-black colours.

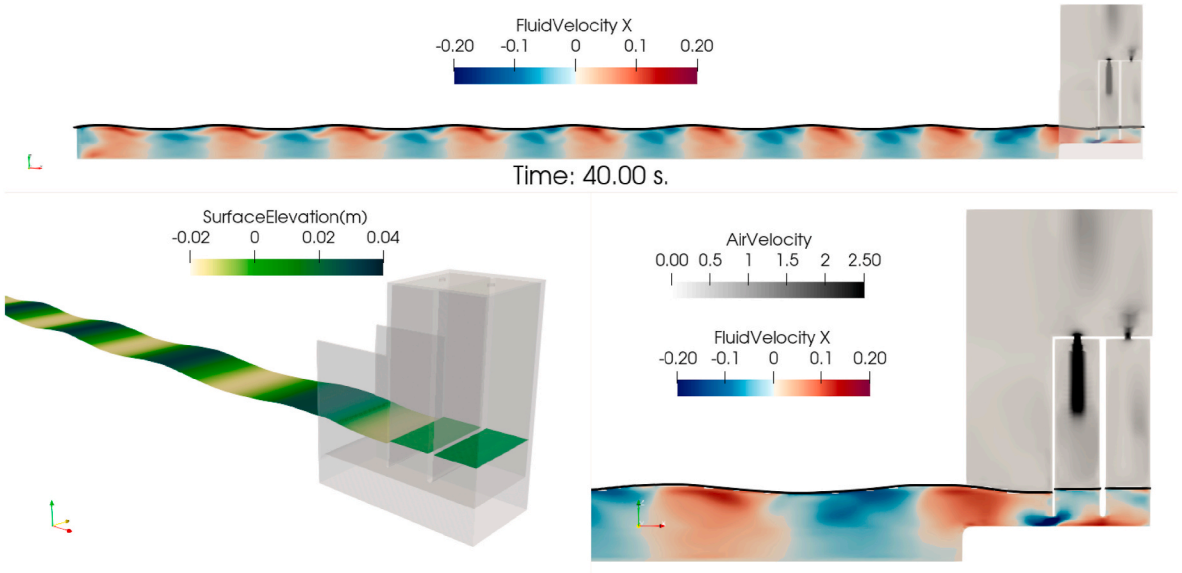

Fig. A1. DCOWC with approach 1 for H = 0.04 m and T = 1.0 s

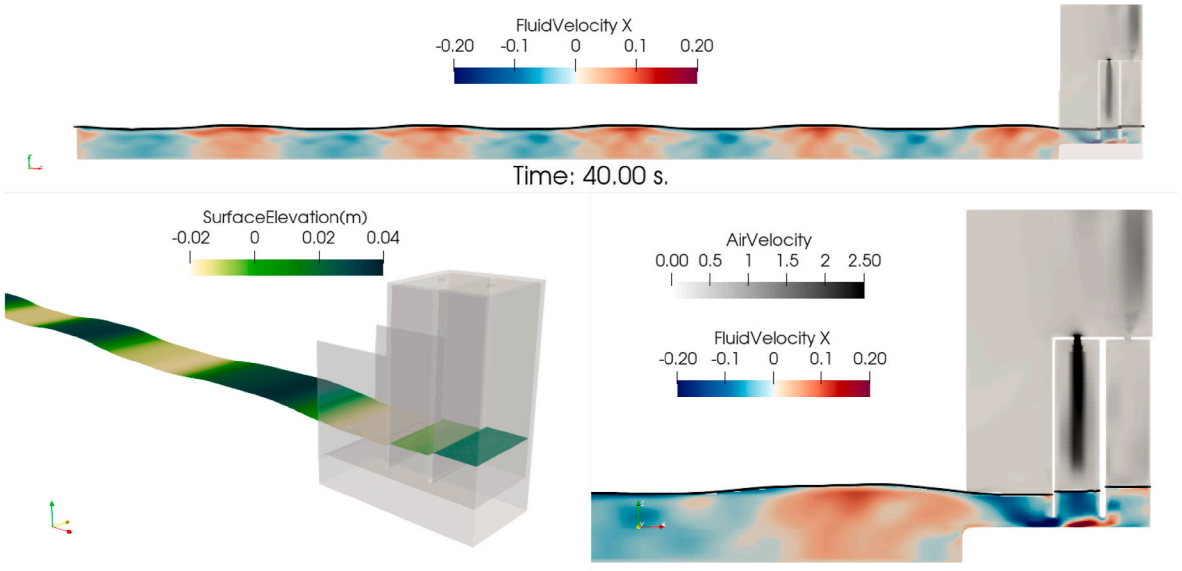

Fig. A2. DCOWC with approach 1 for H = 0.04 m and T = 1.4 s

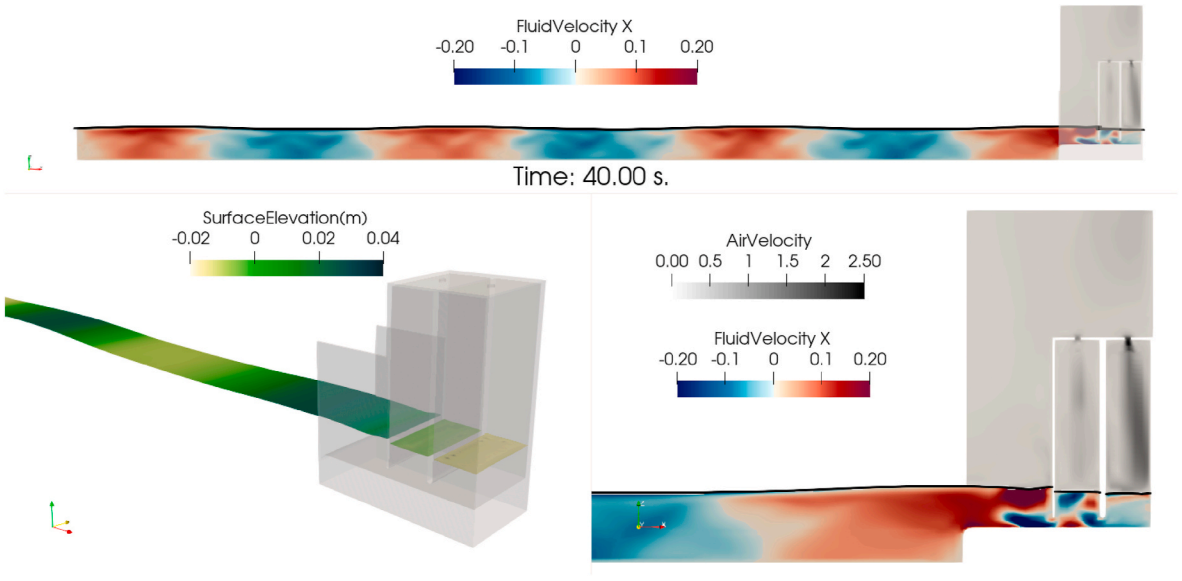

Fig. A3. DCOWC with approach 1 for H = 0.04 m and T = 2.0 s

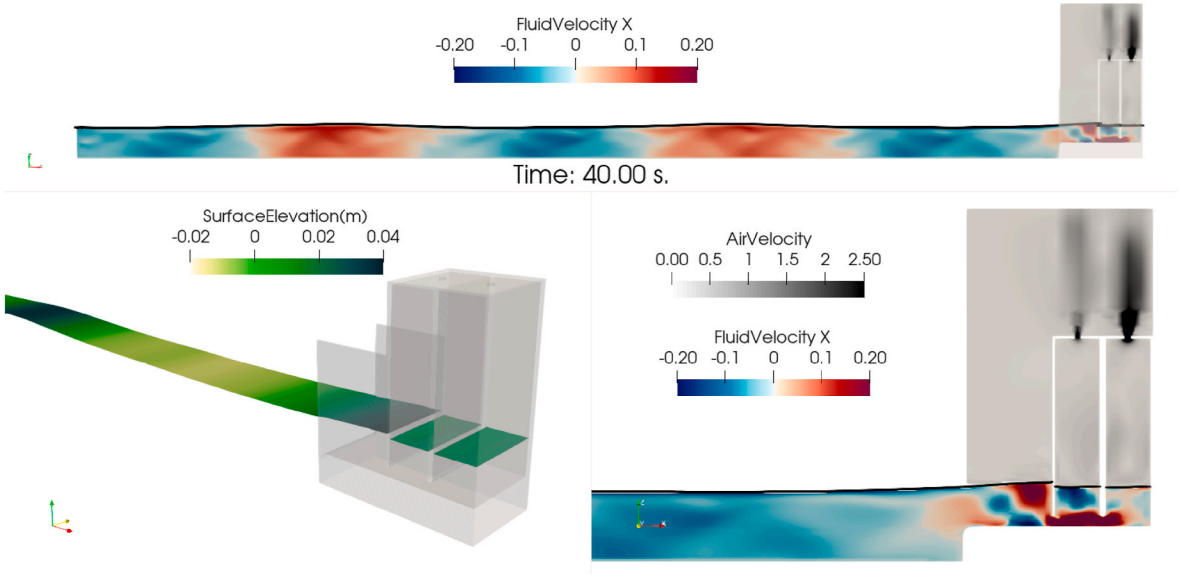

Fig. A4. DCOWC with approach 1 for H = 0.04 m and T = 2.6 s

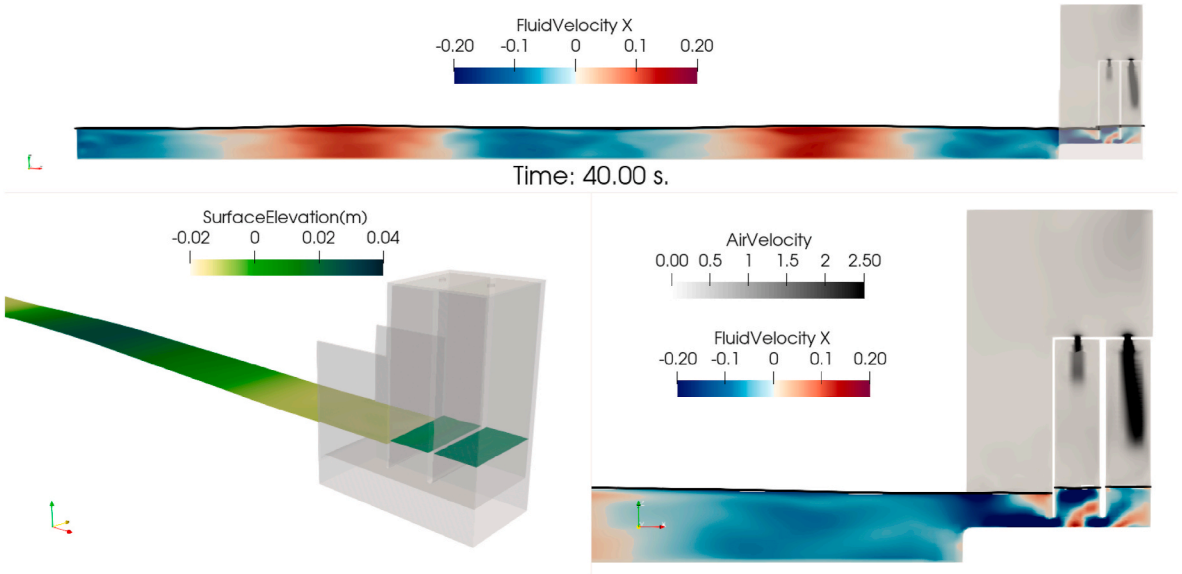

Fig. A5. DCOWC with approach 1 for H = 0.04 m and T = 3.0 s

APPENDIX-B. DCOWC WITH THE PTO MODELLED WITH APPROACH 2

Appendix B presents results (t = 40 s) for the DCOWC, the PTO modelling approach 2 (porous medium), for cases with H = 0.04 m and T = [1.0, 1.4, 2.0, 2.6, 3.0] s, respectively. The top panel is complete NWT, with fluid velocities displayed in red-blue and air velocities in white-black. The bottom left panel, a free-surface elevation in light-dark green colours, and the right panel, a zoom in the vicinity of the dual-chamber OWC, with fluid velocities displayed in red-blue colours and air velocities in white-black colours.

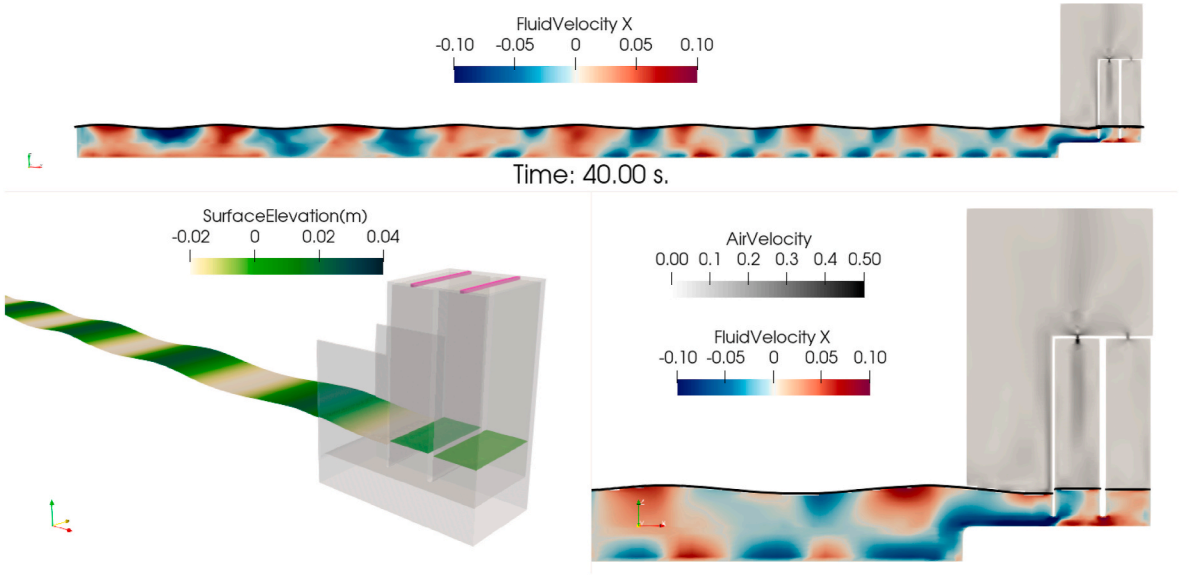

Fig. B1. DCOWC with approach 2 for H = 0.04 m and T = 1.0 s

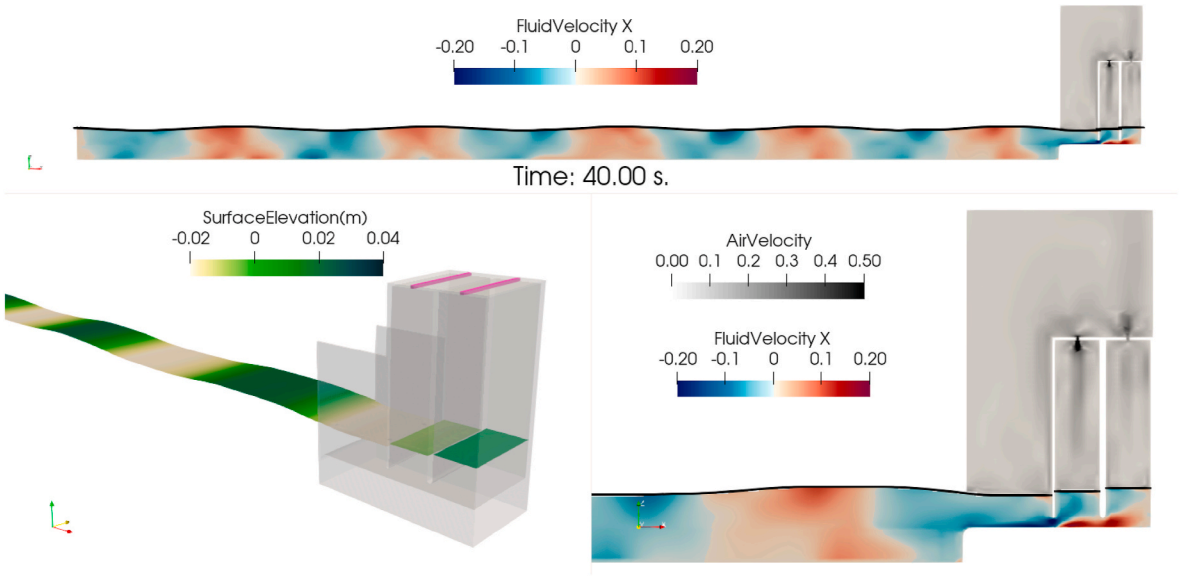

Fig. B2. DCOWC with approach 2 for H = 0.04 m and T = 1.4 s

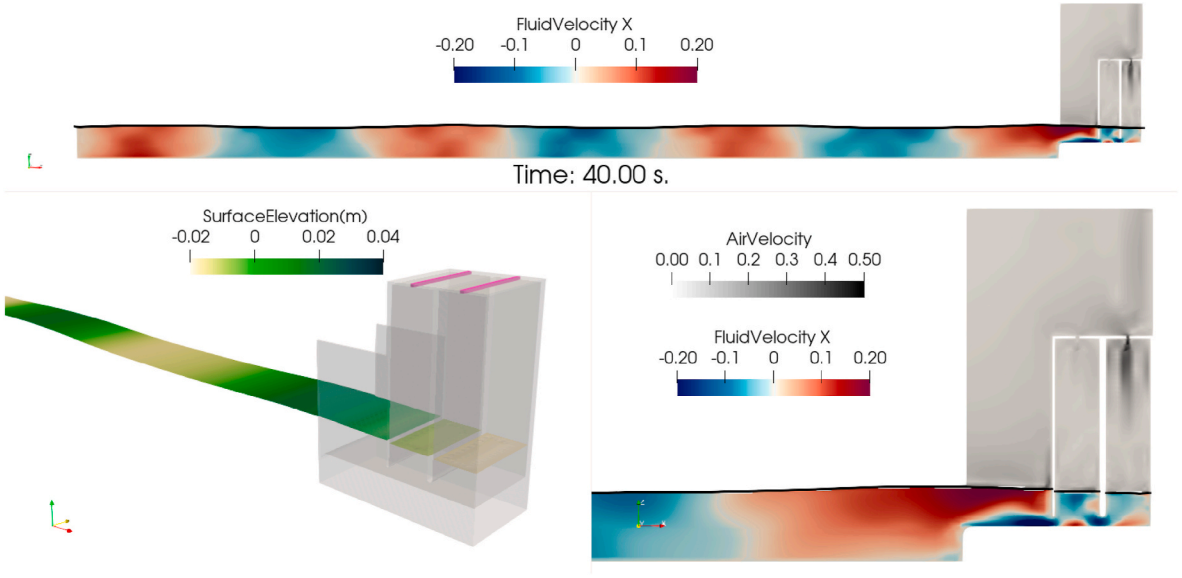

Fig. B3. DCOWC with approach 2 for H = 0.04 m and T = 2.0 s

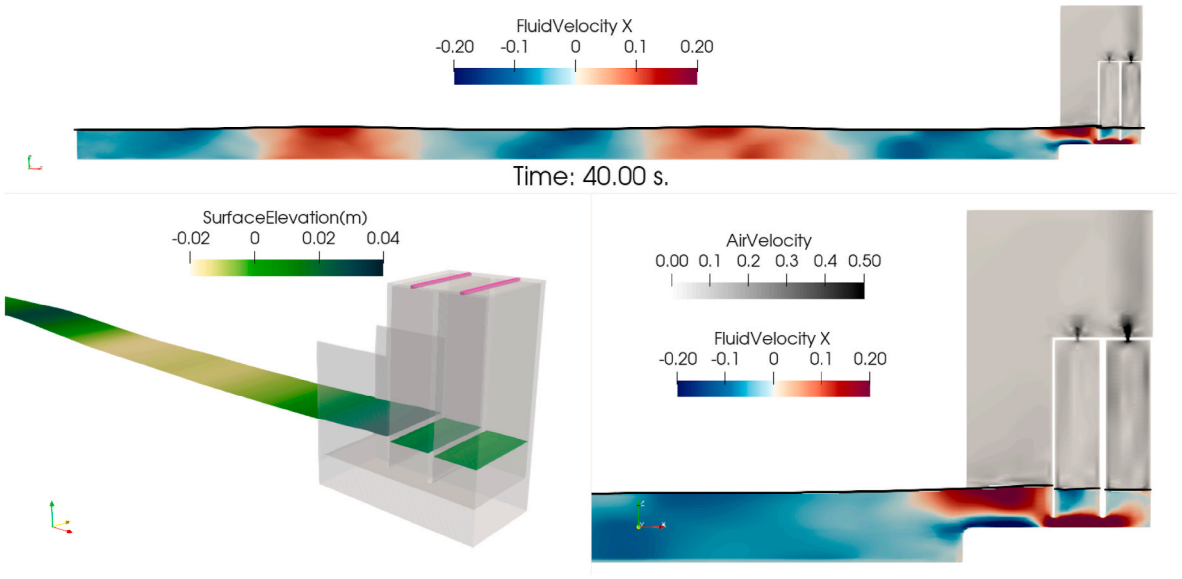

Fig. B4. DCOWC with approach 2 for H = 0.04 m and T = 2.6 s

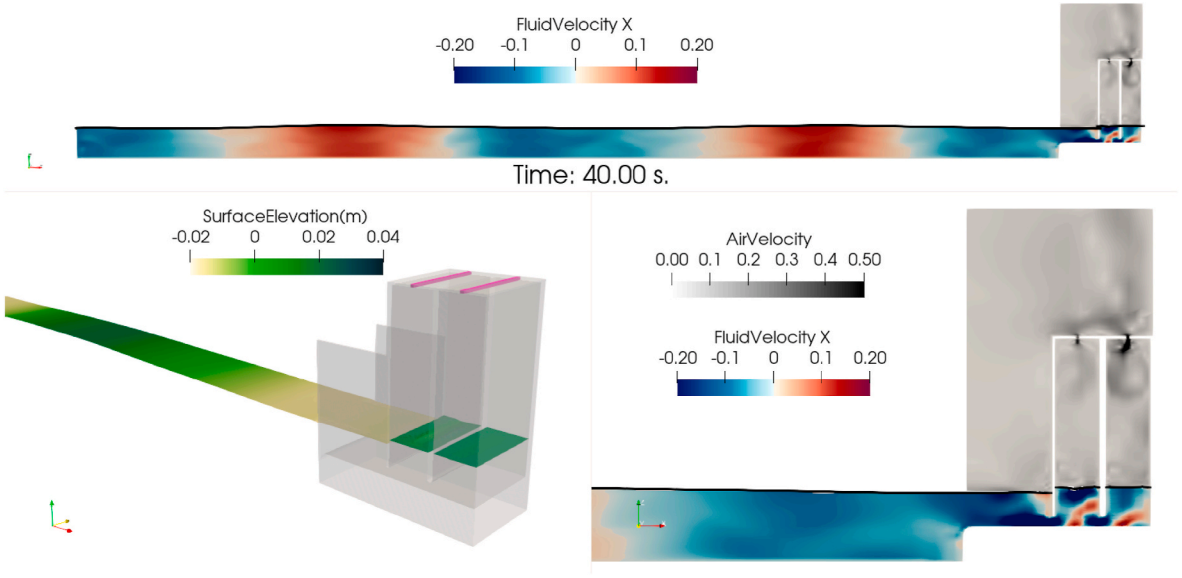

Fig. B5. DCOWC with approach 2 for H = 0.04 m and T = 3.0 s

APPENDIX-C. DCOWC WITH THE PTO MODELLED WITH APPROACH 3

Appendix C presents results (t = 40 s) for the DCOWC, the PTO modelling approach 3 (velocity damping), for cases with H = 0.04 m and T = [1.0, 1.4, 2.0, 2.6, 3.0] s, respectively. The top panel is complete NWT, with fluid velocities displayed in red-blue and air velocities in white-black. The bottom left panel, a free-surface elevation in light-dark green colours, and the right panel, a zoom in the vicinity of the dual-chamber OWC, with fluid velocities displayed in red-blue colours and air velocities in white-black colours.

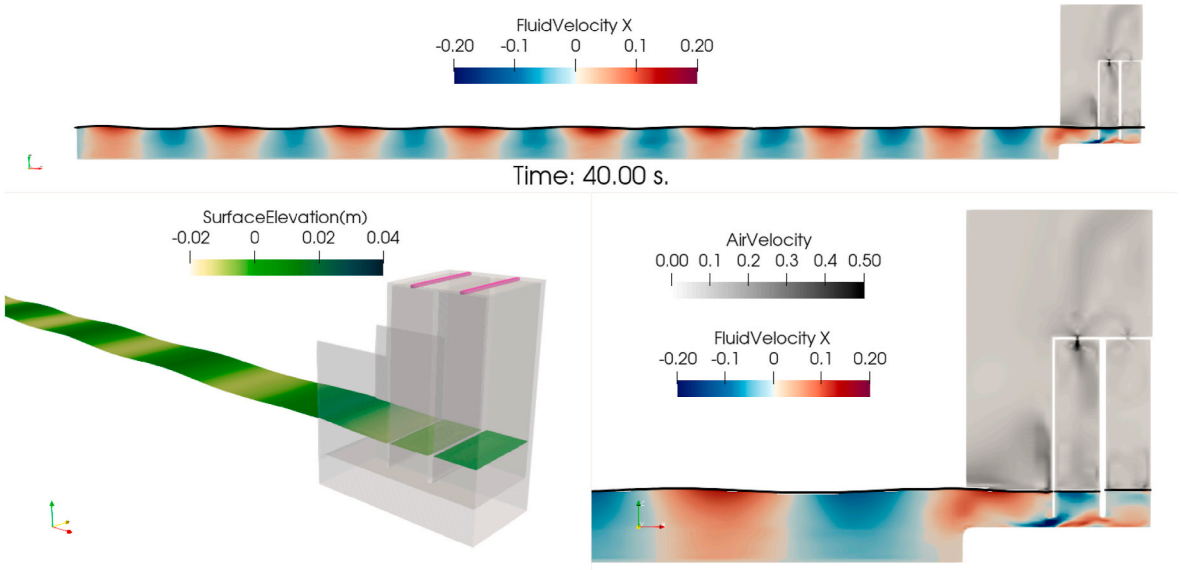

Fig. C1. DCOWC with approach 3 for H = 0.04 m and T = 1.0 s

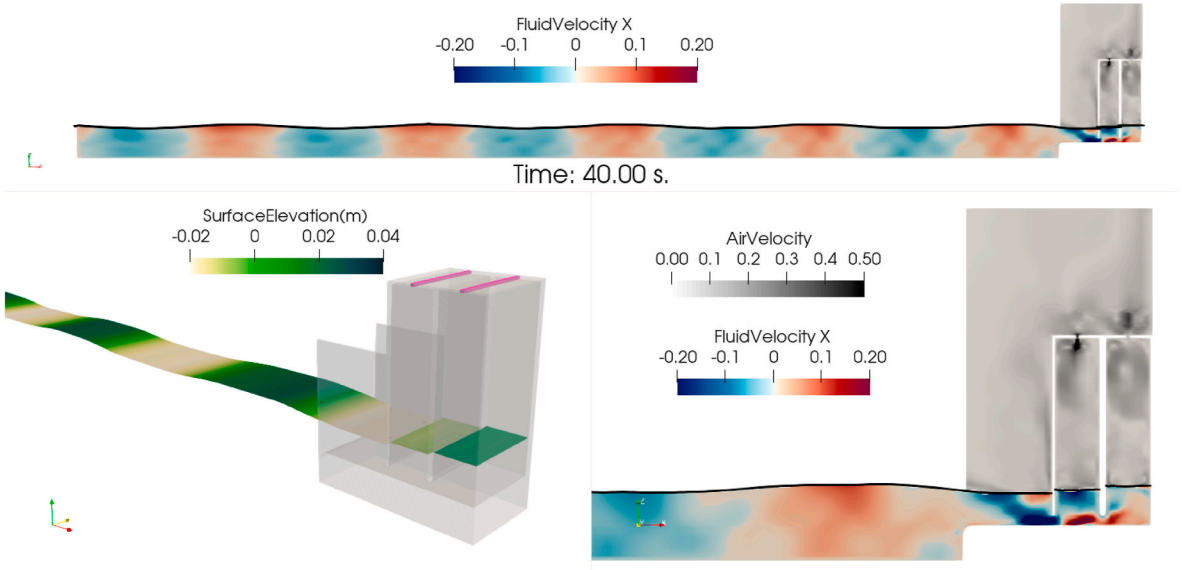

Fig. C2. DCOWC with approach 3 for H = 0.04 m and T = 1.4 s

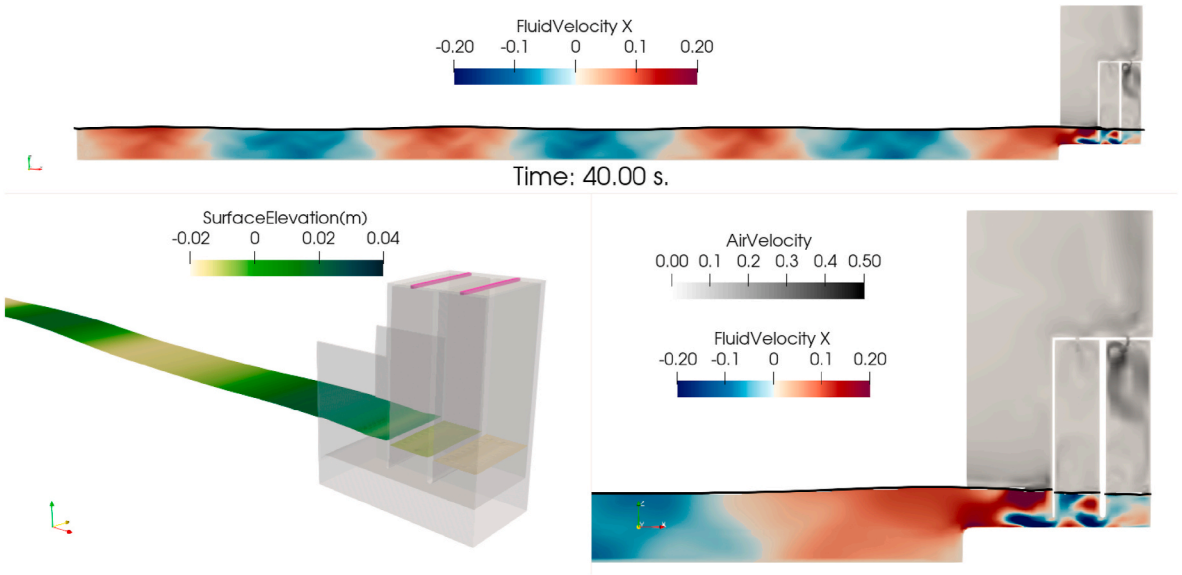

Fig. C3. DCOWC with approach 3 for H = 0.04 m and T = 2.0 s

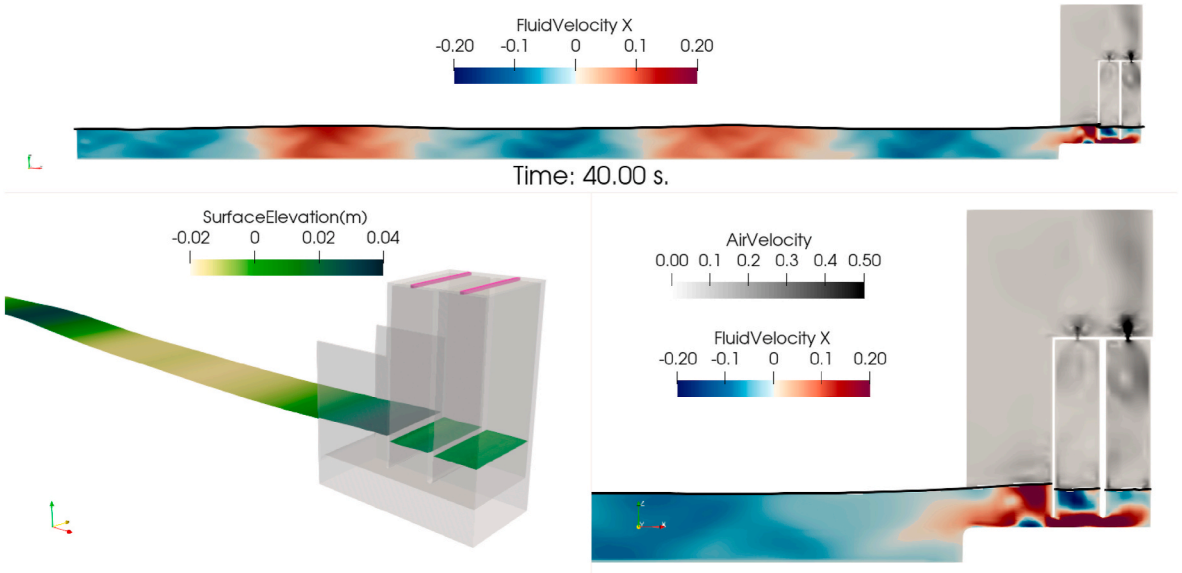

Fig. C4. DCOWC with approach 3 for H = 0.04 m and T = 2.6 s

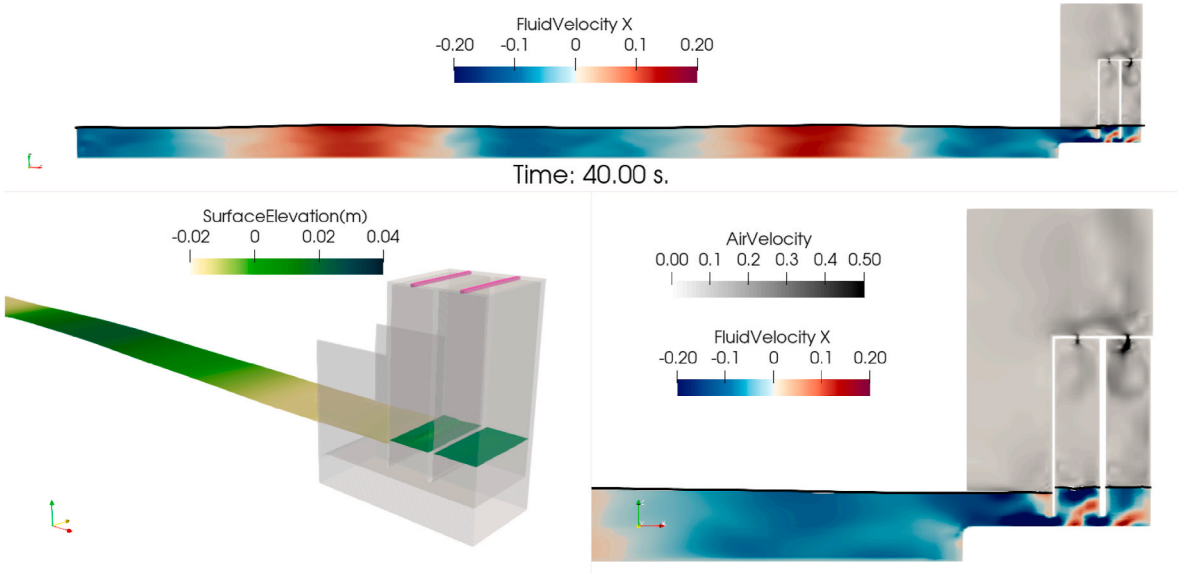

Fig. C5. DCOWC with approach 3 for H = 0.04 m and T = 3.0 s

APPENDIX-D. TCOWC FSE AND AIR VELOCITY FOR A WAVE CYCLE

Appendix D1 depicts snapshots of the vertical velocity in the numerical regions and the FSE representation of a wave cycle for simulation 7 (H = 0.04 m and T = 2.0 s). The case is CFD 0 %, which has low PTO damping in all chambers for the TCOWC and approach 3.

Appendix D2 depicts snapshots of the air velocity streamlines in the holes and the water vorticity representation of a wave cycle for simulation 7, T = 2.0 s, and case CFD 0 % for the TCOWC with approach 1. Simulation time is t = 14.70 s–16.70 s with an interval of 0.25 s between snapshots.

In Figure D1, the red colour in the numerical regions represents a positive air velocity. This means that the compressed air in the chamber is exhaled. If the colour is blue, the chamber is inhaling air from the outside. This happens due to the action of the piston-type behaviour of the FSE. It is visible in Figures D1a) and D1b), where the transition of the wave crest to the wave trough starts, that the first chamber to decompress is the first. At t = 25.10 s (Figure D1e), chamber 1 (the first facing the waves) presents no vertical velocity when the wave reaches its trough.

Observing the contour lines of the vertical velocity in all figures suggests that the air flow rate in chamber 3 is much more pronounced compared to the other two chambers. The middle chamber shows less action. These results align with the air pressure and FSE amplitudes recorded inside the chambers (Figs. 20 and 21), where chamber 2 presents low values. The evident consequence is the low pneumatic efficiency estimated in this chamber (Fig. 22).

As observed and discussed in section 5.3.3, the primary efficiency of the triple-chamber OWC is less than the observed in the dual-chamber OWC. Results of the air flow streamlines combined with the water vorticity in figure D2 for a wave cycle show that the middle chamber works as an obstacle. The water flow shows a significant loss of energy due to the vorticity resulting from the interaction with the internal OWC chamber walls (Figure D2-e).

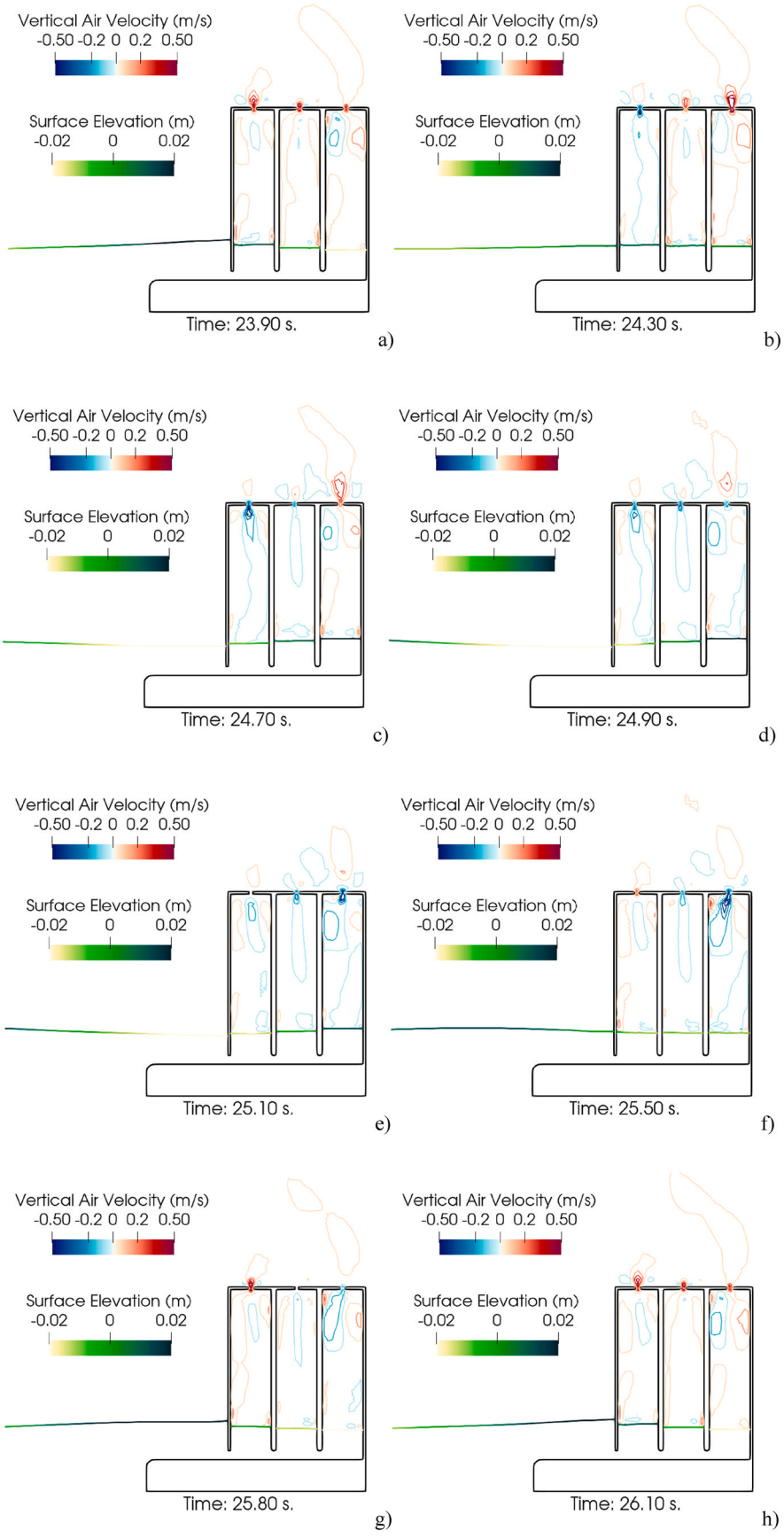

Fig. D1. Snapshots of the vertical velocity in the numerical regions and the FSE representation of a wave cycle for simulation 7, T = 2.0 s, and case CFD 0 % for the TCOWC with approach 3.

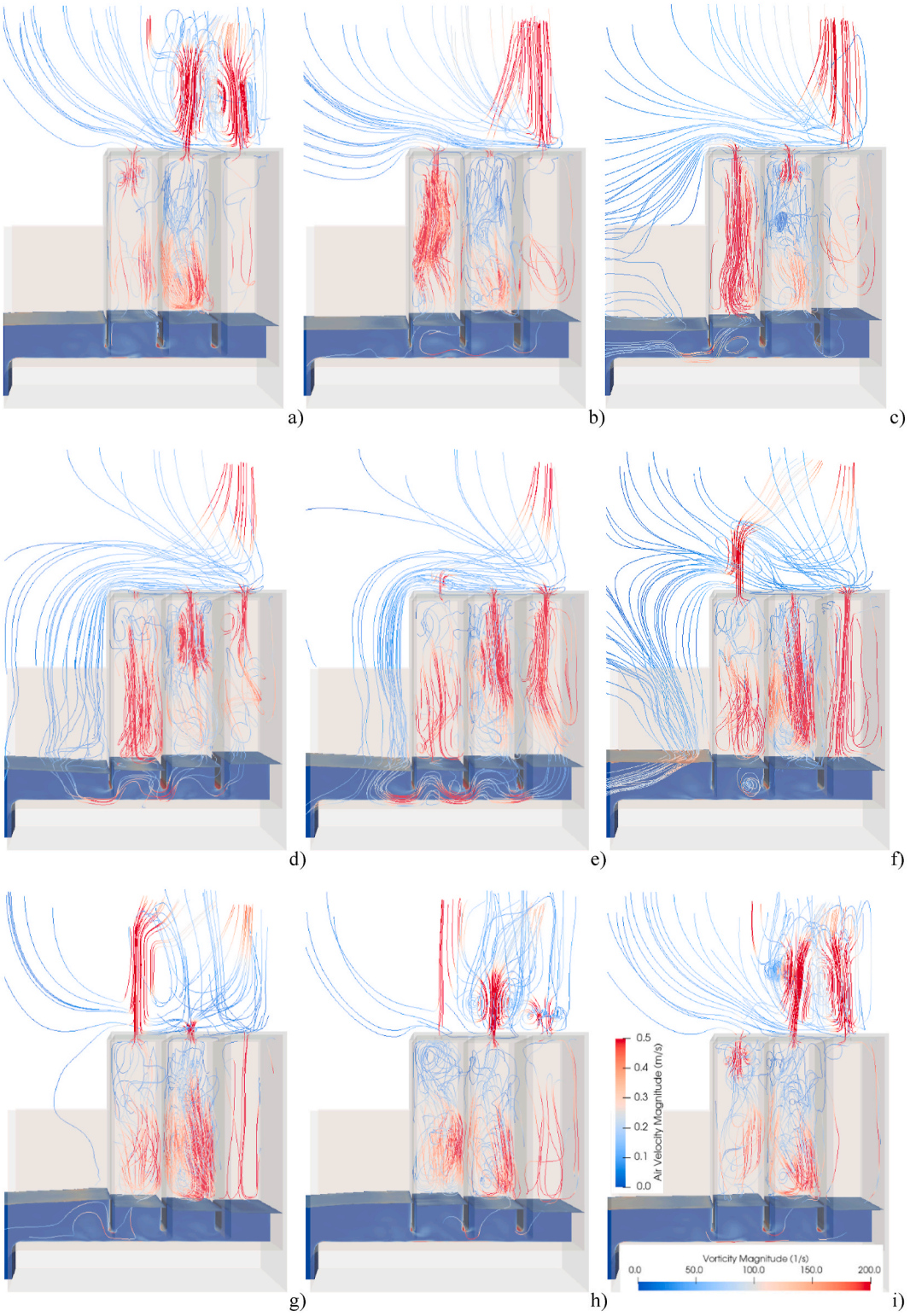

Fig. D2. Snapshots of the air velocity streamlines in the holes and the water vorticity representation of a wave cycle for simulation 7, T = 2.0 s, and case CFD 0 % for the TCOWC with approach 1. Simulation time t = 14.70 s–16.70 s with an interval of 0.25 s between snapshots.

References

Batlle Martin, M., Pinon, G., Barajas, G., Lara, J.L., Reveillon, J., 2023. Computations of pressure loads on an oscillating water column with experimental comparison for random waves. Coast. Eng. 179, 104228. https://doi.org/10.1016/j.coastaleng.2022.104228.

Deng, Z., Wang, C., Yao, Y., Higuera, P., 2020. Numerical simulation of an oscillating water column device installed over a submerged breakwater. J. Mar. Sci. Technol. 25, 258–271. https://doi.org/10.1007/s00773-019-00645-0.

Dimakopoulos, A.S., Cooker, M.J., Lopez, E.M., Longo, D., 2015. Flow characterisation and numerical modelling of OWC wave energy converters. In: Proceedings of the 11th European Wave and Tidal Energy Conference. Nantes, France, p. 8.

Falcão, A.F.O., Gato, L.M.C., Sarmento, A.J.N.A., Brito-Melo, A., 2019. The pico OWC wave power plant: its life from conception to closure 1986-2018. In: Advances in Renewable Energies Offshore. Taylor & Francis, London, UK, pp. 475–483.
Falcão, A.F.O., Henriques, J.C.C., 2019. The spring-like air compressibility effect in oscillating-water-column wave energy converters: review and analyses. Renew. Sustain. Energy Rev. 112, 483–498. https://doi.org/10.1016/j.rser.2019.04.040.
Forchheimer, P.Z., 1901. Wasserbewegungdurch boden. Zeitschrift des Vereins Deutscher Ingenieure 45, 1781–1788.
Gadelho, J., Guedes Soares, C., 2022. Pneumatic performance improvement of an onshore dual chamber OWC using a CFD model. In: Trends in Renewable Energies Offshore. CRC Press, London, pp. 311–318. https://doi.org/10.1201/9781003360773-36.
Gadelho, J., Guedes Soares, C., Barajas, G., Lara, J.L., 2022. CFD analysis of the PTO damping on the performance of an onshore dual chamber OWC. Trends in Maritime Technology and Engineering 2, 381–389. https://doi.org/10.1201/9781003320289-40. CRC Press, London.
Gadelho, J., Rezanejad, K., Guedes Soares, C., 2024a. Experimental and numerical analysis of multi-chamber oscillating water column devices. J. Hydrodyn. 36, 492–503. https://doi.org/10.1007/s42241-024-0043-5.
Gadelho, J., Rezanejad, K., Guedes Soares, C., Santos, J.A., Anastas, G., Fortes, C.J.E.M., 2024b. Experimental study of an onshore dual chamber oscillating water column device. Ocean Engineering 300, 117240. https://doi.org/10.1016/j.oceaneng.2024.117240.
Gent, M.R.A. van, 1995. Wave Interaction with Permeable Coastal Structures. Doctoral Thesis. ISBN 978-90-407-1182-4.
Guedes Soares, C., Bhattacharjee, J., Tello, M., Pietra, L., 2012. Review and classification of wave energy converters. In: Maritime Engineering and Technology. Taylor & Francis Group London, UK, pp. 585–594.
Higuera, P., Lara, J.L., Losada, I.J., 2014a. Three-dimensional interaction of waves and porous coastal structures using OpenFOAM®. Part I: formulation and validation. Coast. Eng. 83, 243–258. https://doi.org/10.1016/j.coastaleng.2013.08.010.
Higuera, P., Lara, J.L., Losada, I.J., 2014b. Three-dimensional interaction of waves and porous coastal structures using OpenFOAM®. Part II: application. Coast. Eng. 83, 259–270. https://doi.org/10.1016/j.coastaleng.2013.09.002.
Iturrioz, A., Guanche, R., Armesto, J.A., Alves, M.A., Vidal, C., Losada, I.J., 2014. Time-domain modelling of a fixed detached oscillating water column towards a floating multi-chamber device. Ocean Engineering 76, 65–74. https://doi.org/10.1016/j.oceaneng.2013.11.023.
Iturrioz, A., Guanche, R., Lara, J.L., Vidal, C., Losada, I.J., 2015. Validation of OpenFOAM® for oscillating water column three-dimensional modelling. Ocean Engineering 107, 222–236. https://doi.org/10.1016/j.oceaneng.2015.07.051.
Kamath, A., Bihs, H., Arntsen, Ø.A., 2015. Numerical modelling of power take-off damping in an oscillating water column device. International Journal of Marine Energy 10, 1–16. https://doi.org/10.1016/j.ijome.2015.01.001.
Keulegan, G.H., Carpenter, L.H., 1958. Forces on cylinders and plates in an oscillating fluid. J. Res. Nut. Bur. Stand. 60.
Kim, J.-S., Nam, B.W., 2022. Numerical analysis for hydrodynamic performance of OWC devices with multiple chambers in waves. J. Ocean Eng. Technol. 36, 21–31. https://doi.org/10.26748/KSOE.2021.091.
Larsen, B.E., Fuhrman, D.R., 2018. On the over-production of turbulence beneath surface waves in Reynolds-averaged navier–stokes models. J. Fluid Mech. 853, 419–460. https://doi.org/10.1017/jfm.2018.577.
López, I., Pereiras, B., Castro, F., Iglesias, G., 2014. Optimisation of turbine-induced damping for an OWC wave energy converter using a RANS–VOF numerical model. Appl. Energy 127, 105–114. https://doi.org/10.1016/j.apenergy.2014.04.020.
Magagna, D., Margheritini, L., Moro, A., Schild, P., 2019. Considerations on future emerging technologies in the ocean energy sector. In: Guedes Soares, C. (Ed.), Advances in Renewable Energies Offshore. Taylor & Francis Group, pp. 3–10.
Mia, M.R., Zhao, M., Wu, H., Palmer, H., 2022. Numerical simulation of a stationary offshore multi-chamber OWC wave energy converter. Ocean Engineering 265, 112546. https://doi.org/10.1016/j.oceaneng.2022.112546.
Ning, D., Ke, S., Mayon, R.B., Zhang, C., 2019a. Numerical investigation on hydrodynamic performance of an OWC wave energy device in the stepped bottom. Front. Energy Res. 7. https://doi.org/10.3389/fenrg.2019.00152.
Ning, D., Wang, R., Chen, L., Sun, K., 2019b. Experimental investigation of a land-based dual-chamber OWC wave energy converter. Renew. Sustain. Energy Rev. 105, 48–60.
Ning, D., Wang, R., Zhang, C., 2017. Numerical simulation of a dual-chamber oscillating water column wave energy converter. Sustainability 9, 1599. https://doi.org/10.3390/su9091599.
Rezanejad, K., Abbasnia, A., Guedes Soares, C., 2020. Hydrodynamic performance assessment of dual chamber shoreline oscillating water column devices. In: Guedes Soares, C. (Ed.), Developments in Renewable Energies Offshore. CRC Press, pp. 188–196. https://doi.org/10.1201/9781003134572-23.
Rezanejad, K., Bhattacharjee, J., Guedes Soares, C., 2015. Analytical and numerical study of dual-chamber oscillating water columns on stepped bottom. Renew. Energy 75, 272–282. https://doi.org/10.1016/j.renene.2014.09.050.
Rezanejad, K., Gadelho, J.F.M., Guedes Soares, C., 2019a. Hydrodynamic analysis of an oscillating water column wave energy converter in the stepped bottom condition using CFD. Renew. Energy 135, 1241–1259.
Rezanejad, K., Gadelho, J.F.M., López, I., Carballo, R., Guedes Soares, C., 2019b. Improving the hydrodynamic performance of OWC wave energy converter by attaching a step. In: International Conference on Offshore Mechanics and Arctic Engineering. American Society of Mechanical Engineers, V010T09A043.
Rezanejad, K., Guedes Soares, C., 2018. Enhancing the primary efficiency of an oscillating water column wave energy converter based on a dual-mass system analogy. Renew. Energy 123, 730–747. https://doi.org/10.1016/j.renene.2018.02.084.
Rezanejad, K., Guedes Soares, C., 2014. Numerical study of a large floating oscillating water column device using a 2D boundary element. In: Developments in Maritime Transportation and Exploitation of Sea Resources. Taylor & Francis Group London, UK, pp. 951–960.
Romano, A., Lara, J.L., Barajas, G., Di Paolo, B., Bellotti, G., Di Risio, M., Losada, I.J., De Girolamo, P., 2020. Tsunamis generated by submerged landslides: numerical analysis of the near-field wave characteristics. J. Geophys. Res. Oceans 125. https://doi.org/10.1029/2020JC016157.
Rosa-Santos, P., Taveira-Pinto, F., Clemente, D., Cabral, T., Fiorentin, F., Belga, F., Morais, T., 2019. Experimental study of a hybrid wave energy converter integrated in a harbor breakwater. JMSE 7, 33. https://doi.org/10.3390/jmse7020033.
Sarmento, A.J.N.A., 1992. Wave flume experiments on two-dimensional oscillating water column wave energy devices. Exp. Fluid 12 (12), 286–292. https://doi.org/10.1007/BF00187307.
Weller, H.G., Tabor, G., Jasak, H., Fureby, C., 1998. A tensorial approach to computational continuum mechanics using object-oriented techniques. Comput. Phys. 12, 620. https://doi.org/10.1063/1.168744.
Xu, C., Huang, Z., 2019. Three-dimensional CFD simulation of a circular OWC with a nonlinear power-takeoff: model validation and a discussion on resonant sloshing inside the pneumatic chamber. Ocean Engineering 176, 184–198. https://doi.org/10.1016/j.oceaneng.2019.02.010.
Zhao, X., Zhang, L., Li, M., Johanning, L., 2021. Experimental investigation on the hydrodynamic performance of a multi-chamber OWC-Breakwater. Renew. Sustain. Energy Rev. 150, 111512. https://doi.org/10.1016/j.rser.2021.111512.